A CONCISE SURVEY OF THE OCCURRENCE AND VARYING FORMATION ENVIRONMENTS OF FELDSPATHIC ROCKS IN THE SOUTHERN HIGHLANDS, MARS

A Thesis
Presented to
The Academic Faculty

by

Alexander M. Sessa

In Partial Fulfillment
Of the Requirements for the Degree
Master of Science in
Earth and Atmospheric Sciences

Georgia Institute of Technology

December 2016

A CONCISE SURVEY OF THE OCCURRENCE AND VARYING FORMATION ENVIRONMENTS OF FELDSPATHIC ROCKS IN THE SOUTHERN HIGHLANDS, MARS

Approved by:

Dr. James J. Wray, Advisor
School of Earth and Atmospheric Sciences
Georgia Institute of Technology

Dr. Yuanzhi Tang
School of Earth and Atmospheric Sciences
Georgia Institute of Technology

Dr. Josef D. Dufek
School of Earth and Atmospheric Sciences
Georgia Institute of Technology

Date Approved: December 8, 2016

ACKNOWLEDGEMENTS

Dr. James J. Wray for his much appreciated advisement throughout the entire M.S. thesis process, helping descope the original proposed study to a more manageable, concise form of equal scientific merit, and useful comments and suggestions that helped produce a better final iteration of this manuscript. Thanks to Dr. Yuanzhi Tang and Dr. Josef Dufek for their thought provoking discussions and reviewing this manuscript prior to submission.

TABLE OF CONTENTS

LIST OF TABLES

LIST OF FIGURES

SUMMARY

Presented here, is a synthesis of previous studies that have resulted in the discovery of feldspathic material on the Martian surface through the utilization of orbital (e.g., OMEGA on Mars Express and CRISM on MRO) and ground based (e.g., ChemCam aboard Curiosity) data sets. Also, presented here for the first time, are additional CRISM detections of feldspar-rich material concentrated in a portion of the southern highlands region of Mars comprised of Noachis Terra, Tyrrhena Terra, and Terra Cimmeria. Possible mechanisms of formation and geochemical formation environments are proposed for the newly observed occurrences based on the localities, and proposed formation mechanisms and environments, of confirmed detections addressed in previous studies. The sites that will be analyzed in depth consist of (1) three infilled, flat-floored impact craters in Noachis, Tyrrhena, and Cimmeria that contain feldspar-rich material within their exposed stratigraphic layers, which is observable in a terraced outcrop, a fractured, light-toned outcrop (igneous or sedimentary in origin), and ejecta surrounding impact craters that sampled the infilling material and (2) a complex crater in Cimmeria with brecciated blocks of feldspar-rich material scattered about its central peak. The IR spectral properties of feldspar, as well as other mineral phases that were found in association with it, are discussed in order to comprehend the conclusions made from the presented remotely sensed data (i.e., CRISM ratioed I/F). The methods employed for CRISM data selection and processing are also emphasized with the resulting data products being introduced and differentiated between.

CHAPTER 1: INTRODUCTION

1.1 Background on Noachian-aged Terrains

It is widely accepted that there was once persistent aqueous activity occurring at the Martian surface. This is substantiated by the presence of water-related geomorphic features (e.g., valley networks [Carr and Head, 2010] and lakes) shaped by precipitation, run-off, and ponding, as well as mineral assemblages that are consistent with aqueous alteration indicative of their geochemical formation environment. The period of time that is most intriguing is the early Noachian epoch (>3.7 Ga), from which the observed presence of phyllosilicate minerals (e.g., (Fe,Mg)-smectites primarily) suggests a long-lived interaction between liquid water of neutral to alkaline pH and rock (i.e., a warmer, wetter Mars). The mineralogic composition of the Noachian-aged southern highlands has been studied extensively by both the Observatoire pour l'Minéralogie, l'Eau, les Glaces, et l'Activité (OMEGA) [Bibring et al., 2005] and the Compact Reconnaissance Imaging Spectrometer for Mars (CRISM) [Murchie et al., 2009b]. These near-infrared data sets have proven to be invaluable in better constraining the composition, setting, and global spatial distribution of seemingly rarer phases (e.g., carbonates, feldspar, hydrated silica, and zeolites) throughout the region in addition to the (Al,Fe,Mg)-phyllosilicates. The Noachian southern highlands represent some of the most mineralogically diverse terrains on the surface of Mars as shown by Mustard et al. (2008), Milliken et al. (2008), Ehlmann et al. (2009), Murchie et al. (2009a), Wray et al. (2009), Ehlmann et al. (2011a, 2011b), and Carter et al. (2013). However, it can be challenging to decide upon a single mechanism of formation is trying to be decided upon for the observed mineralogy. For example, the suggested formation mechanisms for the observed phyllosilicates are (1) alteration of parent materials (felsic to mafic in

composition) by precipitation, runoff, and soil formation, (2) processes associated with top-down leaching, (3) precipitation in situ from fluvial/lacustrine-related processes, and/or (4) hydrothermally driven subsurface alteration related to crustal cooling or impacts.

Currently, it is widely believed that the primary crustal material is basaltic in composition suggesting that magmatic differentiation (i.e., the production of late-stage melts from alkali-rich mantle sources) was not a key contributor to the production of the Martian crust [Mustard et al., 1993; Bandfield et al., 2000; McSween et al., 2009]. As evidence to the contrary, recent meteorite analyses, suggesting the presence of felsic clasts (from monzonitic to granitic in composition) [Humayun et al., 2013; Filiberto et al., 2014], and mission data, suggesting feldspar-rich rocks [Carter and Poulet, 2013; Wray et al., 2013; Sautter et al., 2015], has helped to corroborated early evidence of a more evolved composition being present at the Martian surface (e.g., a dacitic unit in the Nili Patera caldera in Syrtis Major) [Christensen et al., 2005]. These detections, both in situ and remotely sensed, in conjunction with other studies that have reported the presence of localized quartz enrichment from orbit by TES (Thermal Emission Spectrometer) and THEMIS (Thermal Emission Imaging System) [Bandfield et al., 2004; Bandfield et al., 2006; Smith and Bandfield, 2012], possibly point to a more complex geologic history for early Mars and the presence of felsic material (i.e., high alkali and silica content) material.

The study sites being investigated in the southern highlands are mostly flat-floored craters that have been infilled by various processes, which include the transportation and deposition of material from elsewhere on the surface of Mars to its present position when surficial conditions were favorable for aqueous-related weathering

processes (i.e., during the Noachian period). Indeed, if more evolved rhyolitic and/or granitic compositions exist of Mars, such as the recent evidence suggests, then it can be assumed that these infilled craters may contain a stratigraphic record of the emplacement of felsic material.

1.2 Brief Review of Martian Feldspathic Mineralogy (Spectral Fingerprint and Occurrence)

This section will provide a brief synopsis on the spectral properties of feldspar, such as its characteristic absorption feature present in the range of wavelengths considered in this study (i.e., from 1.0 to 3.9 μm, spanning portions of the near-infrared (NIR) and infrared (IR)-wavelength regimes), how physical (i.e., grain size) and chemical (i.e., changes in composition over a solid solution series and substitution of cations within its mineralogic structure) properties affect the shape and strength of the aforementioned absorption, and how the presence of mafic minerals (i.e., olivine and pyroxene) impact its spectral signature. Key spectral features relevant to this study for the zeolite analcime and probable alteration products of feldspar-bearing materials are also discussed succinctly.

The locality, geologic setting, and probable formation mechanism/environment for previous feldspar detections across the Martian surface will be discussed with the primary focus being feldspar occurrences in the southern highlands. This will provide a basis for the interpretations made in the discussion section based on the latest observations of feldspar-rich materials on the surface of Mars being presented here.

1.2.1 Spectral Properties of Feldspar in the Near-infrared

The diagnostic feature that spectrally distinguishes feldspar from other common ferrous iron-bearing silicates (e.g., olivine and pyroxene) with absorptions in a similar wavelength range (1.0 to 1.31 μm) is an absorption centered at ~1.25 μm [Adams, 1975; Adams and Goullaud, 1978; Serventi et al., 2013], which is a result of crystal field transitions in minor amounts of Fe^{2+} substituting for Ca^{2+} ions in seven-coordinated sites within its framework structure [Burns, 2005]. The position, and depth, of the crystal field-related absorption assigned to this substitution can vary depending on the weight percent of FeO, the $NaAlSi_3O_8$ (albite) to $CaAl_2Si_2O_8$ (anorthite) ratio [Adams, 1975], and the particle size. The position can shift tens of nanometers with a minimum occurring at ~1.1 to a maximum at ~1.3 μm [Adams and Goullaud, 1978]. Increasing iron content and particle size affect the near-infrared reflectance spectrum similarly, causing the absorption feature to shift to longer wavelengths and increasing the band depth [Serventi et al., 2013]. For more sodic-rich plagioclase feldspars, the iron content usually decreases, causing the band position to shift to shorter wavelengths and become less apparent. However, as observed for the alkali, as well as Na-dominated plagioclase, feldspar samples contained within the USGS Spectral Library [Clark et al., 2007], they too can have prominent ~1.25 μm Fe^{2+}-related absorption features (e.g., spectra for Albite HS143.3B Plagioclase and Microcline HS103.3B Feldspar specifically, and to a lesser extent Oligoclase HS110.3B and Orthoclase NMNH142137 Fe, which are shown below in Figure 1). This is seemingly explained by Deer et al. (2001) and attributed to the fact that alkali feldspars are a solid solution series varying in composition from pure microcline ($KAlSi_3O_8$) to pure albite ($NaAlSi_3O_8$) in addition to a minor amount of anorthite ($CaAl_2Si_2O_8$), where Ca^{2+} would be substituted for by Fe^{2+}, depending on the temperature and pressure conditions at which the assemblage formed. The effect that

the inclusion of ferrous iron into the structure of plagioclase feldspars has on their VNIR-IR spectra has been investigated in several studies, but its effect on more alkali-rich feldspars has yet to be constrained, which would prove beneficial to the field of Martian minerology.

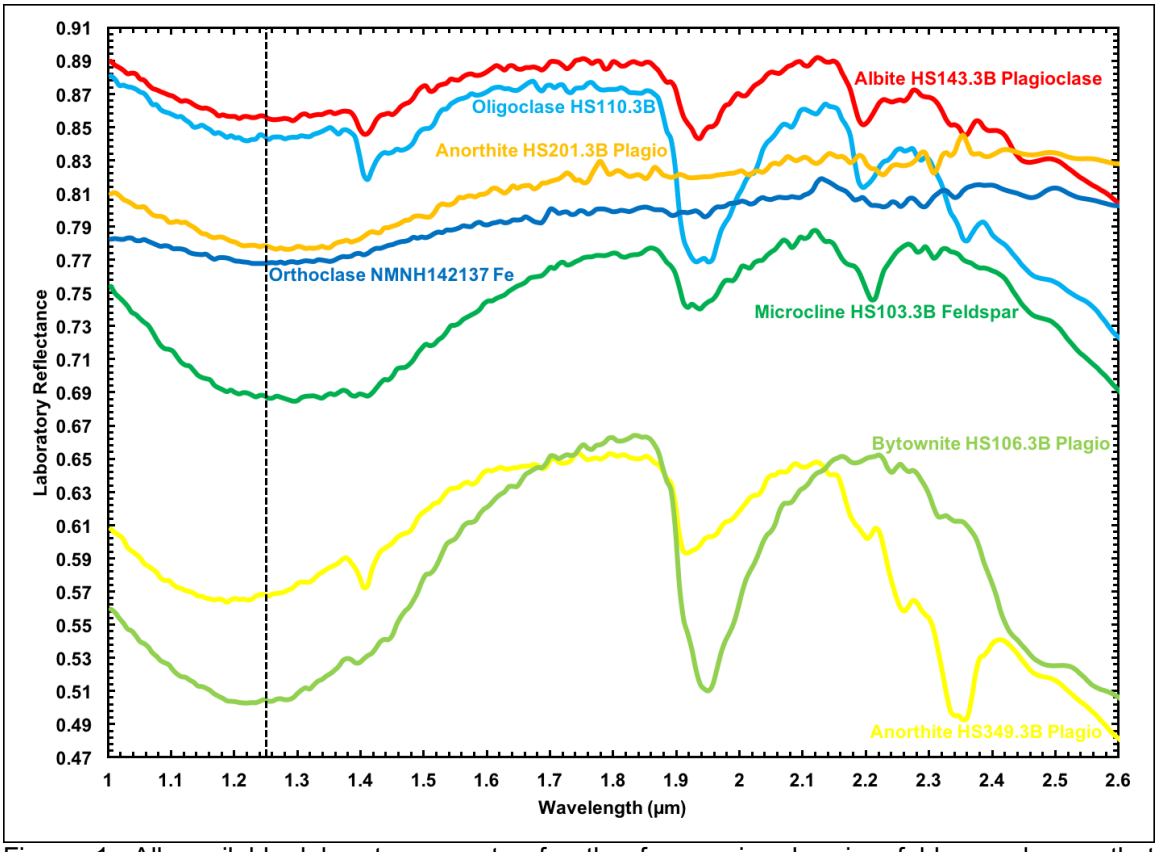

Figure 1: All available laboratory spectra for the ferrous iron-bearing feldspar phases that exhibited the broad ~1.25 μm band (from the Ca-rich plagioclase endmember to the K-rich alkali endmember) contained within the newest iteration of the USGS spectral library, some of which will be used for comparison against ratioed CRISM I/F spectra in this study, are shown here. The black dotted line indicates the position of the previously mentioned absorption feature and is used as a reference for the actual position of the absorptions associated with the different colored feldspar spectra.

The absorption feature discussed in the preceding paragraph has been shown to be only detectable when other mafic constituents are present in abundances of less than 5% [Ohtake et al., 2009; Cheek et al., 2013] or 15% [Nash and Conel, 1974; Crown and

Pieters, 1987] for sub-500 μm feldspar grains, meaning that the host rock would have to be significantly enriched in ferrous iron-bearing feldspar (i.e., compared to other mafic minerals such as olivine and pyroxene) and therefore likely be anorthositic [Carter and Poulet, 2013] or felsic in origin [Wray et al., 2013] to be identifiable in the VNIR-IR spectral range of CRISM. Conversely, in a study by Rogers and Nekvasil (2015), they reported that larger plagioclase phenocrysts (i.e., greater than 840 μm in size) contained within a basaltic groundmass (with up to 50% mafics by volume) can produce a similar spectral feature and thereby call the invocation of felsic lithology into question. It should be mentioned that the mixture used by Rogers and Nekvasil (2015) contained augite with a very high calcium content, which exhibits a broad ~1 μm band attributed to the presence of Ca^{2+} in the M1 site of its single chain structure, thereby swamping out the spectral feature produced by their more sodic feldspar ($Ab_{75}An_{23}Or_2$), which had a smaller percentage anorthite (An) than previous studies and presumably less ferrous iron contained within its structure. This study does however highlight some key spectral properties that are useful when analyzing CRISM spectra, such as the prominent ~1.25 μm absorption attributed to Fe^{2+} within the structure of a feldspar even with a comparatively high Ab/An ratio. It also indicated that other features attributed to alteration (i.e., hydration and hydroxylation) are more appreciable when little to no mafics are present.

1.2.2 Occurrences of Feldspar-rich Material in the Southern Highlands

The localities of previously reported CRISM and in situ ChemCam detections of feldspar-rich material with respect to the southern highlands study region are shown on the Mars Orbiter Laser Altimeter (MOLA) elevation basemap in Figure 2 below.

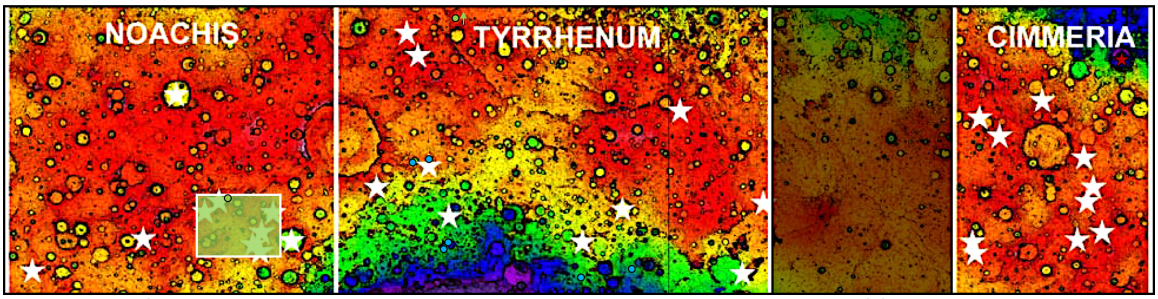

Figure 2: MOLA basemap highlighting previously reported occurrences of feldspar-rich material in the portion of the southern highlands bounded above. The infilled circles (light green and light blue) correspond to the colors of the infilled cells contained within Table 1. The light green box follows a similar color-coding scheme as the circles of the same color.

Feldspar-rich material has also been discovered in other regions of Mars that are not included in the portion of the southern highlands shown. The first reported CRISM observation of this material, which was stated to be most spectrally consistent with bytownite or anorthite (i.e., Ca-rich endmembers of the plagioclase series), was observed in Camichel crater located in Xanthe Terra [Popa et al., 2010], far to the west of the region being discussed in this study and north of Valles Marineris. There have been other detections in the nearby vicinity to the site addressed in Popa et al. (2010) since then by Wray et al. (2013), Carter and Poulet (2013), Ding et al. (2014), and Viviano-Beck (2017). These sites, along with previously reported feldspar-rich material detections located within the study region, are described in Table 1, along with the hydrated minerals detected in association with the feldspar-bearing phases at each locality.

Table 1: The sites where feldspar-rich material has been previously reported are grouped by study and color-coded as on the MOLA basemap depicted in Figure 2. The light purple infilled boxes indicate where feldspathic mineralogy has been identified in the same locality in three different studies. The light blue [Carter and Poulet, 2013] and light green [Wray et al., 2013] infilled boxes correspond to the detections made remotely with CRISM within the southern highlands region (demarcated by light blue and light green infilled circles respectively) defined geographically above. The dark red box indicates where plagioclase to alkali feldspar-rich compositions have been detected in situ with ChemCam within Gale crater (shown in Figure 2 as a dark red star). Also included are the associated alteration, or co-occurring, minerals that were detected in conjunction with feldspar, and each authors' preferred interpretation of feldspar type.

CRISM on MRO							
Study	**Site Description**	**Longitude (°E)**	**Latitude (°N)**	**CRISM Observation**	**Hydrated phases in scene?**	**Hydrated phases mixed with feldspar?**	**Composition of feldspar?**
Popa et al. (2010)	Rim of Camichel crater in Xanthe Terra	-51.66, -51.65	2.71, 2.72	HRL0000985E, HRL0000927F	Yes, (Al,Fe,Mg)-phyllosilicates and hydrated silica	Yes, (Fe,Mg)-phyllosilicates	Bytownite to anorthite
Carter and Poulet (2013)	Rim of Camichel crater in Xanthe Terra	-51.65	2.72	HRL0000927F	Yes, (Al,Fe,Mg)-phyllosilicates and hydrated silica	Yes, (Fe,Mg)-phyllosilicates	Anorthite
	Rim of Holden crater in Margaritifer Terra	-34.24	-27.04	FRT000064B3	No	No	Anorthite
	Rim of unnamed crater in Tyrrhena Terra	62.94	-16.36	HRL0000B5F9	Yes, Al-phyllosilicates	Yes, Al-phyllosilicates (specifically, kaolin-group smectites)	Anorthite
	Rim of unnamed crater in Tyrrhena Terra	64.71	-16.06	FRT0000A26B	Yes, (Al,Fe,Mg)-phyllosilicates	No	Anorthite
	Butte in southern Tyrrhena Terra	66.55, 66.22	-25.37, -25.33	FRT000092B4, HRS0000C6A0	Yes, (Al,Fe,Mg)-phyllosilicates	Yes, Al-phyllosilicates (specifically, kaolin-group smectites)	Anorthite
	Butte in southern Tyrrhena Terra	66.72	-24.61	FRT00013005	Yes, (Al,Fe,Mg)-phyllosilicates	Yes, Al-phyllosilicates (specifically, kaolin-group smectites)	Anorthite
	Butte in southern Tyrrhena Terra	79.42	-28.90	FRT00007D60	Yes, (Al,Fe,Mg)-phyllosilicates and hydrated silica	Yes, Al-phyllosilicates (specifically, kaolin-group smectites)	Anorthite
	Butte in southern Tyrrhena Terra	86.79	-29.70	FRT00018294	Yes, (Al,Fe,Mg)-phyllosilicates	Yes, (Fe,Mg)-phyllosilicates	Anorthite
Wray et al. (2013)	Rim of Camichel crater in Xanthe Terra	-51.65	2.72	HRL0000927F	Yes, (Al,Fe,Mg)-phyllosilicates and hydrated silica	Yes, (Fe,Mg)-phyllosilicates	Felsic rock enriched in plagioclase
	Floor of Nili Patera caldera in Syrtis Major	67.28	8.91	FRT000082EE	Yes, hydrated silica	No	Felsic rock enriched in plagioclase
	Flat-floored crater in Noachis Terra	42.75	-20.25	FRT00008F08	Yes, (Al,Fe,Mg)-phyllosilicates	Possibly, hydration feature barely discernable	Felsic rock enriched in plagioclase
Ding et al. (2015)	Central uplift of Ritchey crater	-50.85	-28.46	FRT00007C34	Yes, (Al,Fe,Mg)-phyllosilicates and hydrated silica	No, however SNR is relatively high for spectral confirmation	Plagioclase
Viviano-Beck et al. (2017)	Canyon wall of Coprates Chasma in Valles Marineris	-55.74	-13.90	FRT0000B8E2	Yes, (Fe,Mg)-phyllosilicates and zeolites (e.g., analcime)	Yes, (Fe,Mg)-phyllosilicates and possibly zeolites (e.g., analcime)	Plagioclase
	Canyon wall of Coprates Chasma in Valles Marineris	-55.59	-14.01	FRT00009804	Yes, (Fe,Mg)-phyllosilicates and zeolites (e.g., analcime)	No	Plagioclase
ChemCam on Curiosity							
Sautter et al. (2015)	Peace Vallis alluvium floats near the northern rim/wall of Gale crater	137.81	5.37	—	—	—	Na-rich plagioclase (e.g., andesine, oligoclase, albite) to K-rich alkali feldspar

1.2.3 Spectral Properties and Formation of Analcime and Other Alteration Phases

Zeolites are characterized by an aluminosilicate three-dimensional framework [Deer et al., 2001] comprising chains of rings of SiO_4 and AlO_4, with the centers of the

cages in the framework structure being occupied by water molecules and other cations (e.g., Na^+, K^+, Ca^{2+}, and Mg^{2+}), the relative concentrations of which play an important role in determining which zeolites are precipitated from solution. The zeolite that will be discussed here, and the one that is found in association with feldspar within the study region, is the Na-zeolite analcime, with a chemical composition of $NaAlSi_2O_6 \cdot H_2O$. Analcime is spectrally distinct from other zeolites in that it is characterized by a strong 2.52 μm absorption most likely due to a spectral feature corresponding to H_2O stretch + bend (AlNa-OH), which increases in depth with increasing Na content [inferred from Cloutis et al., 2002]. Other strong absorptions are observed at 1.42 μm, 1.91 μm, 2.52 μm and progressively weaker absorptions at 1.79 μm, 1.12 μm, 2.14 μm. Analcime was first reported on Mars by Ehlmann et al. (2009), who located it in several small central peak outcrops (i.e., tens of pixels in size) in CRISM images west of Nili Fossae, in complex craters near the Antoniadi basin where it occurs in association with smectite, chlorite, and hydrated silica. The brecciated angular fragments associated with this zeolitic composition are reported as being bright toned rocks underlying a smooth covering material. This zeolite has also been reported in similar complex crater morphologies across the southern highlands by Wray et al. (2009), Ehlmann et al. (2011a, 2011b), and Carter and Poulet (2013), with the same associated mineral assemblage. These assemblages are believed to have been formed by low water/rock impact-generated hydrothermal alteration, or via diagenetic or metamorphic alteration at depth, and then subsequently exposed by impact related processes. This process seems to be favored over the formation of the observed analcime-containing assemblage in saline-alkaline lakes due to lack of observed stratigraphic sedimentary sequences at the surface. In addition, analcime has thus far always been found in association with hydrated silica. A study that supports the possibility of the latter

formation environment (i.e., lacustrine) for analcime is Bristow and Milliken (2011), which discusses the possibility of authigenic (Fe,Mg)-clays forming in situ under alkaline and/or saline conditions in terrestrial lacustrine basins.

Other alteration products that are chiefly observed in the CRISM observations analyzed here are (Al,Fe,Mg)-smectites, kaolins, and hydrated silica, with each having their own distinct spectral properties and mechanisms of formation. As shown in Carter et al. (2013), (Fe,Mg)-phyllosilicates are most common hydrous minerals on Mars, with the specific minerals of this group being most pertinent to this study being (Fe,Mg)-smectites (e.g., nontronite and saponite respectively) and chlorite. The (Fe,Mg)-smectites are 2:1 phyllosilicates (i.e., they consist of a central octahedral sheet of alumina sandwiched by two tetrahedral sheets of silica) and are spectrally identified by the absorption features corresponding to structural H_2O and OH at 1.4 μm, structural H_2O at 1.9 μm, and a ~2.28–2.32 μm feature that changes position from shorter to longer wavelengths depending on the relative proportions of Fe versus Mg (i.e., the center of the aforementioned absorption feature shifts to longer wavelengths as Fe is structurally inserted in place of Mg) [Clark et al., 1990; Bishop et al., 2002]. Often, additional spectrally-resolvable combination tones are present near 2.4 μm. In contrast, chlorites are 2:1:1 phyllosilicates with a T-O-T layer structure (and a brucite-like octahedral interlayer) and display absorption features from 2.2 to 2.5 μm depending on the substitution of cations (e.g., Al, Fe, and Mg) into their layered mineralogical structures. The stronger characteristic absorption at 2.33-2.35 μm is attributed to Mg-OH bonds, with a shift to longer wavelengths associated with increasing iron content (relative to magnesium) within the structure. Also present are weaker features that occur at 2.25-2.26 due to (Al,Fe)-OH or (Al,Mg)-OH stretching modes. For Al-smectites (e.g.,

montmorillonite and beidellite), which were first identified on Mars by Bibring et al. (2006) along with other more common clays, the distinguishing spectral feature is shifted to lower wavelengths than that of (Fe,Mg)-smectites and occurs as a symmetrical absorption near 2.2 μm. This shift in primary band position is attributed to Al being bonded to OH groups within the structure of these clays instead of Fe or Mg. Al-kaolins (e.g., kaolinite, halloysite, and dickite) are differentiated from other Al-phyllosilicates mentioned here by the presence of prominent asymmetric absorptions at 1.4 μm (due to vibrations of interlayer hydroxyl groups) and at 2.2 μm in the form of a doublet (attributed to a combination of vibrations of structurally present Al-OH [Clark et al., 1990]). The absorptions that combine to form the doublet feature are centered at 2.16-2.18 and 2.21 μm. These kaolinite group minerals (formula of $Al_2Si_2O_5(OH)_4$) are classified as 1:1 phyllosilicates with a T-O structure, meaning that they consist of a tetrahedral sheet of silica linked to an octahedral sheet of alumina. (Al,Fe,Mg)-smectites form from weathering (as an authigenic or allogenic sedimentary mineral) or via hydrothermal alteration and are found throughout the Martian southern highlands in association with sedimentary basins (as layered deposits), relatively small craters (as crater wall and central peak exposures and ejecta), and other localities (e.g., Mawrth Vallis and Nili Fossae). Chlorite has a wider range of possible formation environments (e.g., as a primary magmatic mineral, hydrothermally, via metamorphism, or by diagenesis) and is usually, almost exclusively, associated with complex impact craters on the Martian surface, with very few exceptions [Wray et al., 2013].

The final phase that was found in association with feldspar in two out of the four sites analyzed was hydrated silica, which can be classified into the categories of opaline silica (e.g., opal-A or opal-CT) and hydrated, hydroxylated basaltic glass. This phase

exhibits absorption features attributed to Si-OH combination tones at 2.21 to 2.22 μm and at 2.26 μm, assigned to the presence of H-bound SiOH. The position of the absorption band described for hydrated silica overlaps with the diagnostic Al-smectite absorption, however the width of the bands near 2.2 μm for hydrated silica are observably greater in comparison [Milliken et al., 2008]. Additional diagnostic spectral features are observed at 1.91 μm and near 1.4 μm, which can both be attributed to structural H_2O. The ~1.4 μm feature is also due to OH. These features can be somewhat altered depending on the crystallinity of the hydrated silica, thus causing the ~1.4 μm band to shift to longer wavelengths (i.e., from 1.38 to 1.42 μm) and the depth of the 1.91 μm band to increase with increasing crystallinity (i.e., from hydrated glass to opal to quartz) [Rice et al., 2013]. Hydrated silica deposits composed of material with varying degrees of silica crystallinity have been identified in differing localities spanning the southern highlands (e.g., see [Smith and Bandfield, 2013] and references therein), which is believed to be indicative of the geochemical environment in which they originally formed. The currently accepted mechanisms of formation for these deposits are via hydrothermal alteration or diagenesis of mafic crustal materials [Ehlmann et al., 2009; Smith and Bandfield, 2012; Ehlmann and Edwards, 2014].

CHAPTER 2: METHODOLOGY

2.1 Technical Approach and Methodology

This section will explain the technical specifications of CRISM, including the artifacts present in the corresponding dataset and the data processing pipeline, along with creation of summary parameter/browse product maps.

2.1.1 CRISM Data Analysis

2.1.1.1 Technical Specifications

The CRISM instrument is a hyperspectral imager covering the 0.362 to 3.92 μm wavelength range [Murchie et al., 2007] that is used in tandem with the other imaging instruments aboard the Mars Reconnaissance Orbiter (MRO), briefly touched upon later in this section, to spectrally map the exposed mineralogy of the Martian crust. This range of wavelengths is covered by the VNIR (or S) and IR (or L) detectors that span 0.362-1.053 μm and 1.002-3.920 μm respectively [Murchie et al., 2007]. Here, data were analyzed solely from the L detector, primarily in the 1.0 to 2.6-μm range, due to the presence of various distinctive spectral features attributed to hydration, hydroxylation, and crystal field effects within this region [Clark, 1999]. The 3.0 to 4.0-μm region was utilized only when the presence of carbonates was suspected, as these often exhibit strong ~3.4 and ~3.9 μm absorptions; however, hydrated carbonates tend to not clearly

display these C-O overtone features [Cloutis et al., 2000; Ehlmann et al., 2008]. The 3–4 μm region is not typically utilized by itself as CRISM's signal-to-noise ratio (SNR) is more than four times lower at wavelengths longer than 2.7 μm [Ehlmann et al., 2008], and additional out-of-band light leakage was identified in zone 3 of the IR order sorting filter (i.e., roughly 2.8 to 3.9 μm) makes interpretation of this region challenging [Murchie et al., 2007]. CRISM can multispectrally map large swaths of the Martian surface at a spatial resolution of 200 m/pixel while utilizing a subset of 72 selected wavelengths, and can map smaller regions at full spectral and spatial resolution (i.e., 544 spectral bands with 0.00655 μm/channel sampling, at 18-36 m/pixel) in hyperspectral targeted mode.

Two particularly useful resulting data products are the multispectral reduced data records (MRDRs) and targeted reduced data records (TRDRs), which are amassed in multispectral and targeted mode respectively. MRDRs consist of mosaicked map tiles that are constructed from strips of multispectral survey data collected during various orbits [Murchie et al., 2007], while TRDRs provide increased spectral and spatial resolution (i.e., a more "targeted" view) in order to spectrally analyze the regions of interest identified in the MRDRs, or based on other Martian datasets. For this study, TRDRs are primarily utilized in lieu of initial MRDR analysis, due to the prior preliminary determination of the study region (see section 2.2). However, MRDRs could be useful in future studies to approximately determine the spatial extent of possible surficially exposed feldspar-bearing plutonic units first suggested in Carter and Poulet (2013) and Wray et al. (2013). The most recent versions of the TRDRs were used (i.e., TRR3), created using version 3 of the CRISM processing software,

which includes improved calibration procedures to correct many known artifacts and reduce noise through the use of an updated filtering process. The three TRDR data products that were utilized are full resolution targeted (FRT) at 18 m/pixel and half resolution short (HRS)/half resolution long (HRL), both at 36 m/pixel. Full resolution images sample a 10×10 km region, while HRS images are of similar size and HRL images extend to twice their along-track length (i.e., 10×20 km) [Murchie et al., 2009b].

Identified instrument, calibration, and atmospherically-induced artifacts and their corresponding causes are discussed at length in Murchie et al. (2009b). These artifacts can hinder spectral analysis and therefore the CRISM Science Operations team continually works to better correct for them with each new version of the targeted data. The most recently released data products are the preprocessed MTRDRs [Seelos et al., 2011], but they were not utilized here because they are currently available only for select observations. The artifacts that were commonly encountered during this study were the ones occurring at IR wavelengths near 1.65 μm, which can be attributed to the filter boundary between zones 1 and 2, and 2 μm (1.9 to 2.1-μm region), corresponding to correction errors resulting mainly from the inaccurate modeling and removal of the atmospheric CO_2-related absorptions.

2.1.1.2 Data Processing and Selection

The IR data products (i.e., HRS, HRL, and FRT) utilized here were analyzed using ENVI's CRISM Analysis Toolkit (CAT). Prior to this work, these products

had been converted from the raw instrument data with units of DN to I/F, or units of radiance as described by Murchie et al. (2007, 2009b). Over 300 publically-accessed CRISM images from both Google Earth Pro and the CRISM data products map were cursorily analyzed visually using ENVI in conjunction with CAT, which included the pre-analysis steps listed below. CRISM observations that did not have publically available IR data were disregarded prior to the use of CAT.

1) The IR/VNIR image data (TRR3) files, along with the IR/VNIR geometric information (DRR1) files, are downloaded and stored in the same folder for the sake of organization.
2) The PDS-format TRR3 file is then converted to a CAT-format file, so that it can be processed via CAT.
3) The CAT file is then atmospherically corrected by removing the contribution of the atmosphere utilizing the volcano scan correction method, which makes use of an atmospheric transmission spectrum previously derived from observations at the base and summit of Olympus Mons. For a particular CRISM observation the atmospheric transmission spectrum is scaled to match the band depth of the 2-μm CO_2 feature in each pixel, and then the observed spectrum is divided by this scaled spectrum. This procedure, which assumes a multiplicative atmospheric contribution to Martian surface spectra, removes absorption features stemming from atmospheric gases with few resulting residual artifacts; however, aerosols (such as dust and ices) and other gases such as water vapor are not independently corrected for, and may lead to spectral slopes or minor residual absorptions [McGuire et al., 2009; Ehlmann et al., 2009; Morgan, 2011].

4) The CAT file is simultaneously photometrically corrected by dividing by the cosine of the incidence angle. By assuming that, to first order, the surface behaves as a Lambertian scatterer, this process ultimately corrects for the variation in viewing geometry from observation to observation.
5) The atmospherically and photometrically corrected spectral cubes are then map projected.
6) Summary parameters (for both IR and VNIR), as defined by Pelkey et al. (2007) and Viviano-Beck et al. (2014), are then calculated from the resulting atmospherically and photometrically corrected spectral cubes. These parameters highlight certain mineral-related spectral features; this process is further elucidated in section 2.1.1.3.
7) The summary parameters are then "flattened", which removes column-oriented banding and corrects the "spectral smile" artifact that plagues pushbroom-type imaging spectrometers [Murchie et al., 2007; Ceamanos and Douté, 2010].
8) These flattened summary parameters are finally map projected and ready to be used in tandem with the projected spectral cubes in order to locate potential regions of interest (ROIs).

After analyzing all the processed CRISM images using the aforementioned procedure, spectral cubes that were deemed too noisy or where localized materials were too difficult to detect (mostly HRS images) were discarded.

2.1.1.3 Summary Parameters and Map Synthesis

2.1.1.3.1 Spectral Parameters and Browse Products

The CRISM multispectral (and hyperspectral) summary products originally proposed by Pelkey et al. (2007), and then revised and supplemented by Viviano-Beck et al. (2014), allow for the spectral identification of many different mineral phases exposed at the Martian surface. As a whole, this suite of spectral parameters is designed to determine the spatial distribution and variation of minerals that are associated with unique spectral signatures across the surface of Mars. Specifically, each individual parameter is constructed with a particular purpose in mind; to detect a particular reflectance peak (inverse band depth parameter), absorption (band depth parameter), or multiple absorptions (doublet and two-band parameters) that are characteristic of a particular mineral phase, on a pixel by pixel basis. A number of these parameters had been used in studies prior to CRISM's arrival at Mars, such as those performed using data from the OMEGA instrument to map Martian minerology. The newest iteration of the CRISM spectral parameter summary products that were utilized in this study can be found in Viviano-Beck et al. (2014), which contains a table that includes the name of the parameter (both abridged and full), its formulation, and its scientific rational (and caveats). The combinations of CRISM spectral parameters that were utilized as "summary (browse) products" in this study are shown in Table 2.

The general formulation of the band depth parameters is explained in Pelkey et al. (2007) and is exemplified by Equation 1 below. The primary function of this specific parameter is to calculate the band depth of a spectral feature relative to a sloped linear spectral continuum (dotted line on the plots shown in Figure 3), which is defined by two anchor points (demarcated as *S* and *L*), positioned on either side of the absorption feature. This spectral slope,

connecting anchor points *S* and *L*, is a representation of the expected shape of the spectrum over a specified wavelength range in the absence of the absorption of interest. It is mathematically determined by the change in reflectance (ΔR, $R_1 - R_2$) over the change in wavelength ($\Delta\lambda$, $\lambda_1 - \lambda_2$) for a particular portion of the spectrum. The band depth (i.e., the depth of the absorption) is represented by the following equation.

$$BD(\lambda_C) = 1 - \frac{R_C}{R_{C^*}} = 1 - \frac{R_C}{aR_S - bR_L} \quad (1)$$

Where *a* is defined as 1-*b*, *b* is equal to $(\lambda_C - \lambda_S)/(\lambda_L - \lambda_S)$, and R_S, R_L, and R_C are the reflectances at the wavelengths corresponding to points *S*, *L*, and *C* in the spectrum [Pelkey et al., 2007]. R_{C^*} is the reflectance value along the dotted sloped continuum at wavelength *C*, corresponding to the center of the absorption band. The weighting parameters (*a* and *b*) are crucial in the detection of minerals with asymmetric absorption features, which are not centered halfway between the two anchor points (such as the particular case shown in Figure 3A, where the center of the absorption is positioned closer to *L*). The band depth, which is calculated using Equation 1, is generally proportional to the amount of a certain mineral phase within a CRISM pixel, however other factors such as the particle size and the albedo of the material can alter the shape and depth of the resulting spectral feature [Clark and Roush, 1984; Pelkey et al., 2007].

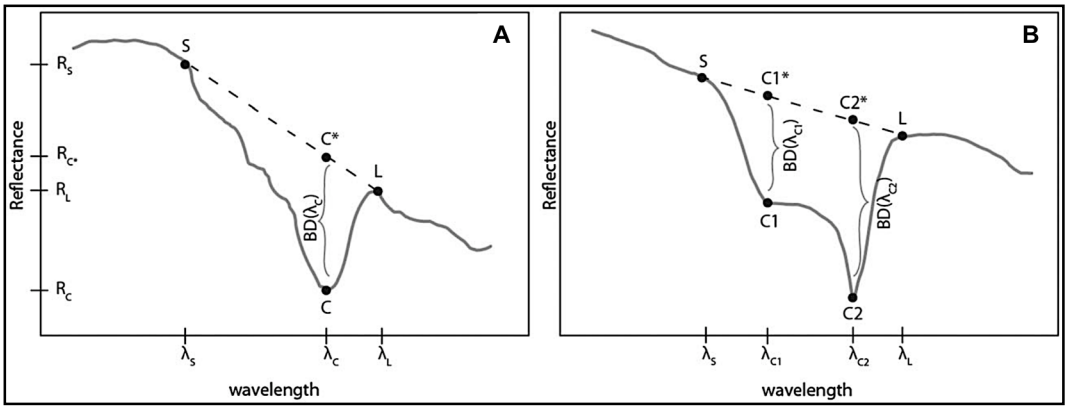

Figure 3: Panel A depicts the formulation described above, while panel B depicts a doublet absorption feature common to kaolin-type minerals. Adapted from Viviano-Beck et al. (2014).

However, the functionality of these spectral parameters goes beyond being able to simply identify and map a single mineral phase with a particular absorption or set of absorptions. These parameters can be used in conjunction with one another to produce browse products, which are 8-bit scaled RGB (i.e., red, green, blue) color composites that display three-band combinations of thematically related summary products [Viviano-Beck et al., 2014]. This allows for better visualization of the spatial distribution of materials present in the CRISM image cube being analyzed. These browse products also allow for a more accurate identification of a particular mineral phase (i.e., beyond merely knowing if a mineral is hydrated or not, it can in tandem be identified as an Al, Fe, or Mg-smectite based on other characteristic absorption features). The relevant browse products utilized in this study are further defined in Table 2 (including their abbreviations, RGB components, and significance/implications).

Table 2: Abbreviation, RGB components (colored for clarity), and the significance (as well as the importance) of the browse products used in this study. TRU, MAF, and PHY were previously defined by Viviano-Beck et al. (2014). The CUSTOM browse products are unique to this study and allow for better visualization of exposed surface material that contains feldspar, alteration products plus feldspar, or feldspar with associated mineral phases.

Abbreviation	RGB Components	Significance and Interpretation
TRU (True Color)	R600	An enhanced true color representation of the scene, derived from I/F after correction for atmospheric and photometric effects.
	R530	
	R440	
CUSTOM 1	BD1300	Feldspar-rich material appears red when unaltered or not copresent with another mineral phase and yellow when altered or co-occurring with another phase (e.g., (Fe,Mg)-phyllosilicates or zeolites). Olivine, (Fe,Mg)-phyllosilicates, and zeolites appear green and olivine appears cyan when in occurrence with pyroxene. Blue represents both low- and high-Ca pyroxene.
	BDI1000IR	
	BDI2000	
MAF (Mafic Mineralogy)	OLINDEX3	Olivine and Fe-phyllosilicates appear red in the MAF browse product. Low- and high-Ca pyroxene appear green or cyan depending on the position of the center of the absorption (i.e., the closer the feature is to 1.81 µm the greener the appearance and as the absorption shifts to longer wavelengths it appears more cyan in color) and blue or magenta depending on the compresence of olivine.
	LCPINDEX2	
	HCPINDEX2	
PHY (Phyllosilicates)	D2300	(Fe,Mg)-OH bearing minerals (e.g., (Fe,Mg)-phyllosilicates) appear red or magenta when hydrated. (Al,Si)-OH bearing minerals (Al-phyllosilicates or hydrated silica) appear green or cyan when hydrated. Blue colors indicated other hydrated phases (e.g., sulfates, hydrated silica, or water ice). Mg-carbonates appear magenta in some instances.
	D2200	
	BD1900R2	
CUSTOM 2a	BD1300	Feldspar-rich material appears red when unaltered or not copresent with (Fe,Mg)-phyllosilicates, yellow when altered to (or co-occurring with) (Fe,Mg)-phyllosilicates, and bright yellow to white when hydrated. (Fe,Mg)-phyllosilicates appear green or cyan when hydrated, while all other hydrated phases (e.g., Al-phyllosilicates, sulfates, hydrated silica, or water ice) appear blue. Mg-carbonates may appear magenta.
	D2300	
	BD1900R	
CUSTOM 2b	BD1300	Feldspar-rich material appears red when unaltered or not copresent with zeolites (specifically, analcime) and bright white when co-occurring with zeolites (analcime). Green colors are indicative of Mg-carbonates and some zeolites (analcime) with cyan indicating the presence of the characteristic ~1.9 µm-absorption. Other hydrated phases (e.g., Al-phyllosilicates, sulfates, hydrated silica, or water ice) are shown in blue.
	BD2500_2	
	BD1900R	
CUSTOM 2c	BD1300	Feldspar-rich material appears red when unaltered, yellow when bound water is structurally present, and bright white when partially altered (i.e., hydrated). Material containing bound water appears green and hydrated material or, more likely, pyroxene-rich material with an absorption centered near 1.9 µm appear blue.
	BD3000	
	BD1900R	

2.1.1.3.2 Spectral Parameter Mapping

Mineralogical maps are created by utilizing the parameters and browse products described in the previous section. As previously stated these maps allow for the visualization of a specific mineral phase, or an assemblage of minerals, present within a CRISM observation by highlighting a pixel, or groups of pixels, within the scene that exhibit certain spectral features unique to that specific area, or multiple areas throughout the image. Greyscale parameter maps can be produced by utilizing the spectral parameters individually, thereby allowing for the identification of various outcrops throughout the image that

display a similar, singular absorption feature prescribed by the parameter being invoked. By contrast, a browse product depicts three summary products at once with each corresponding to a different color channel in a RGB-composite image. These types of maps better show the spatial relationship between various different minerals present in a single scene, as well as indicating if any regions within the image being analyzed contain a localized mixture of mineral phases, which is spectrally characterized by multiple absorptions being present in the spectrum collected from that area. Browse product maps can also better constrain the presence of a particular mineral phase, whose characteristic spectrum is composed of more than just one absorption feature (i.e., both Al-smectites and Fe/Mg-smectites display a ~1.9 μm feature but they differ in that one has a ~2.2 μm feature and the other a ~2.3 μm feature, respectively, which correspond to different metal-OH bonds present within their structure). This process is illustrated below in Figure 4 with the resulting map-projected summary product/browse product maps being shown in the middle panels and the map-projected, photometrically and atmospherically corrected CRISM observations on the left.

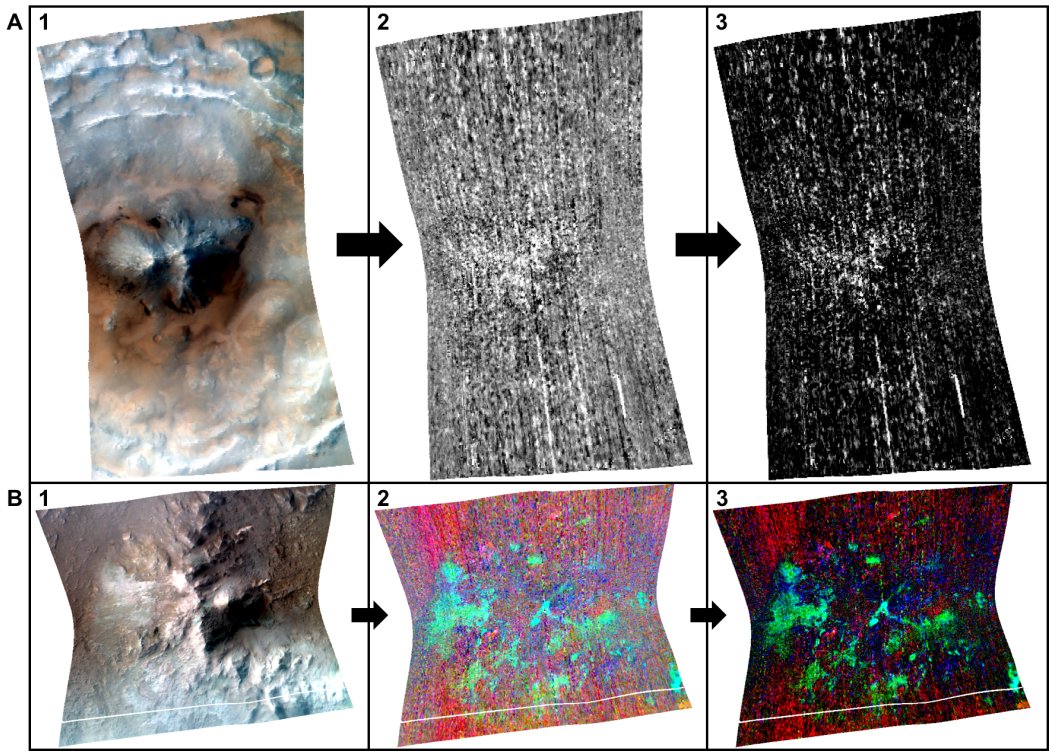

Figure 4: (A1) through (A3) and (B1) through (B3), for summary and browse product maps respectively, exemplify the stretching process that was utilized throughout this study to identify ROIs from the vast expanse of pixels in each CRISM observation (i.e., A2 and B2 show the standard stretch, treating the resulting pixel values as a normal distribution and truncating the lowest and highest two percent, while A3 and B3 show the stretch described below). (A1) is the corrected observation HRL000082E3, with (A2) and (A3) created from it using the BD1900R2 parameter. (B1) is the corrected observation FRT00003A2B, with (B2) and (B3) produced from it by utilizing the PHY browse product.

For both summary and browse products, the resulting maps were produced by utilizing an optimum stretch that was determined to best spatially show the distribution of a specific mineral phase, or set of minerals, respectively within the CRISM observation. The stretching process is illustrated above in Figure 4 and is accomplished by visually inspecting the histogram that corresponds to the distribution of pixel brightness throughout the image and choosing to only display the brightest pixels (i.e., from the distribution maximum [mode] to the ~99th percentile). This accentuates pixels within the image that yield high values for the calculated summary parameters and blacks out, or

subdues the brightness of, any pixels with values that are below the scene average. This process also helps to greatly subdue spurious bright pixels that result from detector, or atmospherically, induced noise spikes that erroneously yield high pixel values and visually interfere with the interpretation of the produced maps. However, these noise-induced bright pixels are only truly eliminated if a median filter in applied. The results of this stretching process are shown above for both summary product (A, top panels) and browse product (B, bottom panels) maps in the right most panels of Figure 4 being stretched as previously described.

The aforementioned maps not only allow for the visual representation of spectrally distinct materials contained within the image, but also facilitate subsequent manual inspection of the pixels contained within these regions for attribution to a specific mineral phase, or phases, based on their IR spectra. Regions of interest (ROIs) are chosen (manually or automatically) based on where, within an image, the summary products yield a localized increase in pixel brightness. These ROIs can range in size, from tens of pixels to hundreds of pixels, and shape (i.e., ellipse, rectangle, polygon, or a combination of multiple ellipses/rectangles), depending on the spatial extent of a spectrally distinct unit. When averaging over larger ROIs, features can be subdued if pixels contained within the chosen region do not have the same spectral attribute. On the other hand, if too few pixels are chosen, thermal noise from the CRISM detector and/or Martian atmospheric features will drown out the diagnostic spectral features from the surface. Furthermore, simply examining the spectral average of the chosen pixels typically does not allow for clear identification of the distinctive material(s) in that region, due to noise originating from the previously mentioned sources

and probable mixing of other materials (e.g., globally widespread dust) within the selected ROI. The method employed here (and in most CRISM analyses published to date) to mitigate artifacts and emphasize diagnostic spectral features is the division by a spectrally bland denominator (i.e., a neighboring ROI, of similar size, that is positioned in the same column of pixels in the unprojected, atmospherically corrected CRISM spectral cube as the numerator ROI). This method thereby allows the resulting ratioed spectra to be analyzed and identified via comparison to the compiled spectra of mineral phases contained within the USGS Spectral Library [Clark et al., 2007].

2.2 Defining the Selected Region of Study

The mineralogical composition of wind-eroded floor materials, as well as exposed stratigraphic layers and other corresponding geological units, contained within and located in close proximity to (i.e., within ~100 km of the crater rim of) thirty Noachian-aged impact craters in the Martian equatorial highlands (between 0–30°S, 0–165°E) was investigated by utilizing the CRISM instrument aboard MRO. Geographically, the abovementioned subset of craters lies to the north of Hellas Basin and spans three different regions of the Martian surface, which includes Noachis Terra (20–55°E), Tyrrhena Terra (55–100°E), and Terra Cimmeria (120–140°E). The study region in its entirety is shown below in Figure 5.

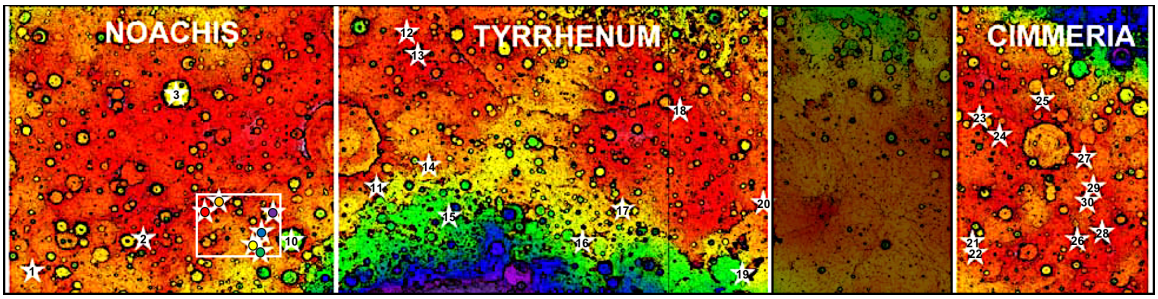

Figure 5: The study sites (i.e., thirty flat-floored craters) are demarcated by the numbered white stars and binned into their respective labeled study areas, which are superimposed on a MOLA basemap and bounded by 0°S, 30°S, 20°E, and 140°E. Lower topographic features are shown in cooler colors (green, blue) and more prominent features are shown in warmer hues (orange, red). The white box shows the spatial extent of the study region from Wray et al. (2013) and its location within the region being examined here. The sites demarcated by the colored circles correspond to unnamed craters contained within the aforementioned region of study and correspond to sites 4 (red), 5 (orange), 6 (yellow), 7 (green), 8 (blue), and 9 (purple) in this study. No craters were chosen for analysis in the blacked out portion of the map.

These sites were selected through a survey of flat-floored craters by R. P. Irwin III, who documented all available MRO imaging, which includes that from the CRISM instrument with a resolution of 18 (or 36) m/pixel (as previously stated) [Murchie et al., 2007, 2009b], Context Camera (CTX) with a resolution of 6 m/pixel [Malin et al., 2007], and the High Resolution Imaging Science Experiment (HiRISE) with a resolution of 0.25 m/pixel [McEwen et al., 2007]. As a whole, the study region partially overlaps a portion of the southern highlands surveyed by Wray et al. (2009), as well as the region investigated by Wray et al. (2013) where multiple exposures of feldspar-rich material were reported and spectrally confirmed. Furthermore, this region constitutes some of the least dust-covered areas in the southern highlands [Ruff and Christensen, 2002], allowing for relatively unobscured views of the composition of materials that comprise the Noachian-aged terrain.

CHAPTER 3: RESULTS

3.1 Graphical Breakdown of Feldspathic Material Observed in Study Region

The sites where feldspar-rich material was detected span the entirety of the region of study from site 2 to 30. Each detection that we confirmed spectrally is discussed below. The locations of the previous detections occurring within the defined study region are included in the MOLA basemap shown in Figure 6 along with the additional detections being presented here, which were added to the map originally shown in Figure 2. Two of the craters where unaltered feldspars were detected contain no associated alteration products and occur in close proximity to mafic minerals (e.g., olivine and pyroxene). However, the other two detections occur in the presence of a suite of hydrated phases and concurrently with the zeolite analcime and with alteration products (specifically, (Fe,Mg)-phyllosilicates).

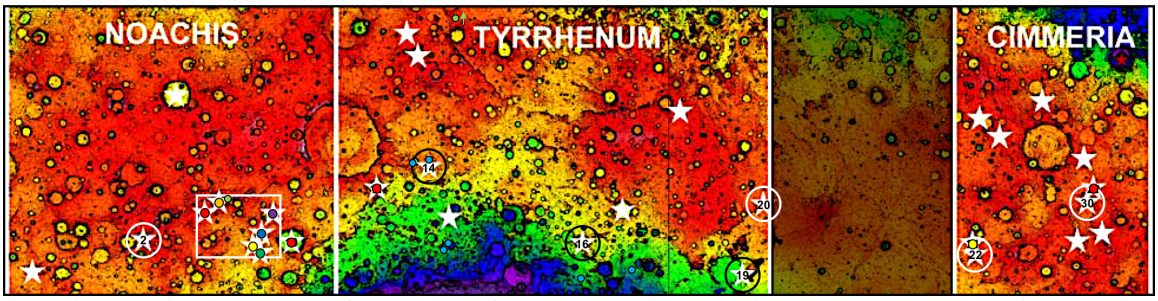

Figure 6: Revised version of the map of the study region shown in Figure 5 displaying where feldspar has been previously identified remotely from orbit using CRISM and through in situ chemical analyses by ChemCam, a laser-induced breakdown spectrometer (LIBS), aboard Mars Science Laboratory (MSL) rover Curiosity. The white circles encompassing the numbered stars demarcate the sites from this study where previously unidentified feldspar-rich outcrops were remotely sensed using CRISM. The white box defines the boundaries of the study region from Wray et al. (2013) with the light green infilled circle representing the approximate location of the spectrally-confirmed, feldspar-rich material identified therein and the circle directly north of crater 14 (with an accompanying arrow of a similar color) corresponds to the light-toned, feldspar-rich unit observed in the Nili Patera caldera of Syrtis Major. Carter and Poulet (2013) identified several other occurrences of feldspar throughout the southern highlands, which are shown by light blue infilled circles. The in situ detection of feldspar-rick rock of magmatic origin found in Gale crater is denoted by a dark red star and is from the study conducted by Sautter et al. (2015). The

numbered crater sites encircled in black represent tentative feldspar detections but are not discussed at length in this study. The craters with red circles concealing them located outside of the Wray et al. (2013) region were not analyzed fully and are therefore not considered.

3.2 Identification, Mapping, and Occurrence of Feldspar with Associated Phases

3.2.1 Noachis Terra

3.2.1.1 Crater 2 (Unnamed)

An unnamed crater, labeled site 2 in Figure 5 and 6, bounds the western extent of the feldspar-bearing material that was observed and confirmed spectrally within the study region. The feldspathic material observed in this scene occurs as unaltered outcrops (shown as red in Figure 7B), as well as in an altered form (shown as yellow in the same figure). The spectra presented in Figure 8 sample the region pointed to by the white arrow in Figure 7A. A bland denominator was located at the base of the altered outcrop specified in panel A and then two ROIs where chosen of the same size and in the same line of pixels to determine if the resulting ratioed spectra allowed for the differentiation between altered and unaltered feldspar-rich material. A third numerator ROI was chosen that encompassed the entirety of the region bounded horizontally by the aforementioned numerator ROIs to see if the resulting spectral ratio behaved as expected. As expected the spectral ratio between the ROI consisting of pixels that exhibited no signs of hydration (represented as red in the CUSTOM 2a browse product defined previously and depicted in panel E) and the bland ROI produced a spectrum that had a broad absorption centered at ~1.3 μm, and was relatively flat from ~1.8 μm to 2.6 μm compared to the other ratioed spectra presented in Figure 8. When compared to other studies that investigated the effects that composition and grain size have on

position and depth of the ferrous iron induced feldspar feature, this spectrum appears to signify a material that contains Ca-rich plagioclase (e.g., bytownite or labradorite) due to the absorption being positioned at a longer wavelength. The red spectrum was produced from a numerator ROI comprised of pixels that are shown as bright white in Figure 7E; this produced a spectrum with absorptions at about 1.4, 1.9, 2.3, 2.4, and 2.5 μm, along with a narrower feature positioned near 1.25 μm rather than at 1.3 μm. This can be interpreted several different ways due to the current ambiguity of the effects that chemical and physical properties have on the position of the Fe^{2+} feature in feldspar spectra. However, it can be suggested that the Ca-rich endmembers that once comprised a substantial portion of the rock have been removed during aqueous alteration, leaving behind a rock that is now enriched in more Na-rich plagioclase, ferrous iron enriched plagioclase, and the alteration product that spectrally resembles a (Fe,Mg)-smectite mixed with other (Fe,Mg)-phyllosilicates. The green spectrum behaves as would be expected, with an intermediate absorption centered around 1.28 μm and hints of hydration/alteration.

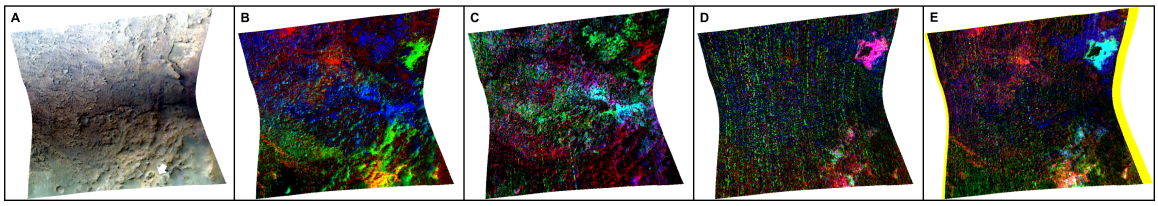

Figure 7: (A) shows an enhanced true color representation of FRT00009665, while the subsequent browse product maps allow for the visualization of the feldspar-bearing material located in the southeastern corner of the scene, which is indicated by a white arrow. (B) and (C) reveal the relationship between the presence of feldspar and mafic phases, while (D) and (E) show associated hydrated phases (e.g., (Al,Fe,Mg)-phyllosilicates and hydrated silica) present in this image. The browse products being shown here are TRU (A), CUSTOM 1 (B), MAF (C), PHY (D), and CUSTOM 2a (E).

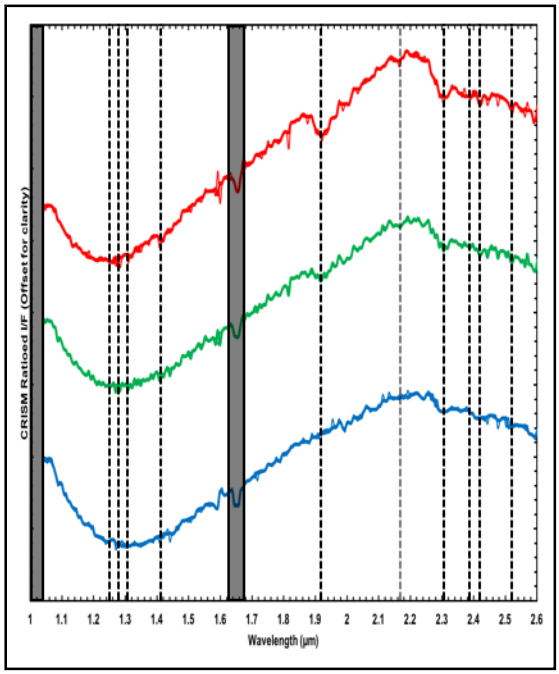

Figure 8: Ratioed CRISM I/F from ROIs within the region indicated by the white arrow in Figure 7. This CRISM observation is located in the southeastern corner of an unnamed, flat-floored crater in northeastern Noachis Terra. The blue spectrum is more indicative of a relatively unaltered feldspar-bearing protolith and the red spectrum shows spectral features that are consistent with alteration. Both the red and blue spectra were collected from ROIs of the same size in the same columns of pixels while utilizing the same denominator. The green spectrum was produced by creating an ROI encompassing the entire region horizontally bounded by the two previous ROIs, which yielded a spectrum with a ~1.28 μm absorption positioned between those of the red and the blue, along with subduing the alteration features present in the red spectrum. The spectra presented here are offset for clarity, and the gray boxes indicate where spectral data were disregarded due to detector boundary-related issues (1 to ~1.04 μm and ~1.65 μm).

3.2.2 Tyrrhena Terra

3.2.2.1 Crater 20 (Unnamed)

The observation analyzed in this section covers a central peak located within a crater with a diameter of ~17 km positioned to the northwest of Kamativi (crater 20 in this study). The outcrops highlighted by arrows in Figure 9A appear bright white in the CUSTOM 2b browse product map in Figure 9E, which indicates they exhibit strong absorption features near 1.3, 1.9, and 2.5 μm. The spectra that correspond to these

regions are shown in Figure 10A and, from 1.4 to 2.6 μm, both are almost completely identical to the USGS spectrum for analcime shown in panel C of Figure 10. Specifically, the absorptions that are present in both the laboratory spectrum and CRISM I/F spectra occur at approximately 1.42 μm, 1.91 μm, 2.52 μm. Other, albeit weaker, characteristic absorptions present in the laboratory spectrum for this particular zeolite occur at 1.79 μm, 1.17 μm, and 2.14 μm, with the first being barely resolvable and the latter two not being resolved in the CRISM spectra, which is due to the weakest bands being the first to disappear at the SNR achievable by CRISM as mineral abundance decreases [Ehlmann et al., 2009]. However, the absorption present at ~1.25 μm is unaccounted for by the laboratory spectrum for analcime and must be attributed to the presence of another mineral phase within the outcrop being examined. The most logical interpretation of this feature is the co-presence of feldspar. As previously discussed, the position of the ~1.25 μm band center is not as diagnostic as would be desired here, but when considering the chemical composition of analcime it can be postulated that the feldspar that is co-occurring with this Na-zeolite is more sodic than calcic. Within this particular image analcime is found in relatively small light-toned outcrops of brecciated rocks in and around the central peak, which is consistent with the observations of analcime made at other locations on Mars by Ehlmann et al., (2009, 2011a, 2011b) and Wray et al. (2009). It appears to be exhumed from a smooth covering material that is spectrally distinct from the blocks of inferred analcime/feldspar reported here. Possible formation mechanisms for this composition will be discussed in the next section. The other diagnostic hydrated minerals that are present in this scene are (Al,Fe,Mg)-phyllosilicates (possibly smectites), hydrated silica, Mg-carbonates (tentative), and other zeolites.

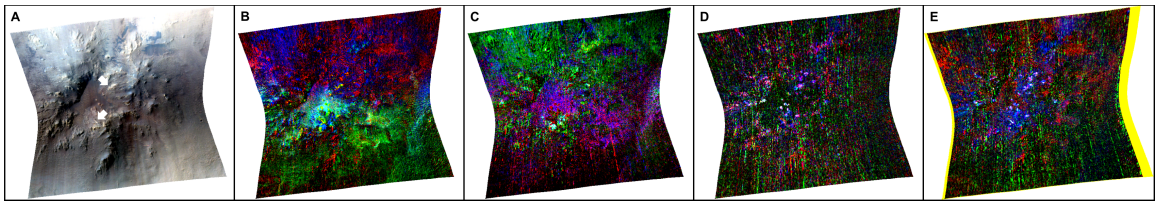

Figure 9: (A) shows an enhanced true color representation of FRT00009E58, while the following browse product maps allow for the visualization of the two spectrally confirmed feldspar-bearing outcrops in the imaged central peak, which are indicated by white arrows. Again, (B) and (C) reveal the relationship between feldspar-rich material and mafic phases, while (D) and (E) show the presence of co-occurring zeolites (e.g., analcime) and other associated hydrated minerals (e.g., (Al,Fe,Mg)-phyllosilicates and hydrated silica) contained within the scene. The browse products being shown here are TRU (A), CUSTOM 1 (B), MAF (C), PHY (D), and CUSTOM 2b (E).

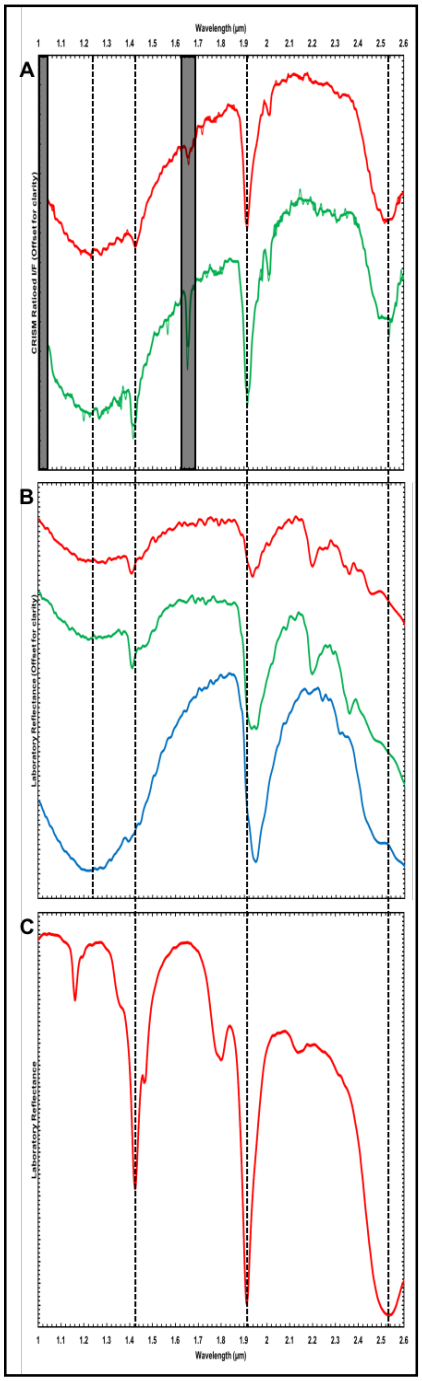

Figure 10: (A) CRISM ratioed I/F spectra from FRT00009E58 (unnamed central-peaked complex crater neighboring Kamativi to the northwest) in southeastern Tyrrhena Terra, interpreted as consistent with sodic/alkaline feldspar plus the zeolite analcime. (B) USGS laboratory spectra for minor Fe^{2+}-substituted albite, oligoclase, and bytownite. (C) USGS laboratory spectra for analcime for comparison with the ~1.4 μm to 2.6 μm region of the CRISM ratioed spectra shown in (A). The red spectrum in (A) originates from the white arrow to the south in Figure 9A, while the green spectrum corresponds to outcrop identified by the northernmost arrow. All spectra are vertically offset for clarity, and the gray boxes in (A) denote where spectral data was disregarded due to detector boundary-related issues (1 to ~1.04 μm and ~1.65 μm). The adjacent CRISM observation (FRT0000C339), imaging the more eastern portion of the central peak, spectrally confirms the presence of the same material in the same locations.

3.2.3 Terra Cimmeria

3.2.3.1 Crater 22 (Unnamed)

The crater that was imaged in this CRISM observation (HRL0001C492) is located at the western edge of the Terra Cimmeria portion of the study region and represents our only observed occurrence of polygonally fractured, light-toned material similar to that originally reported in the region defined by Wray et al. (2013) in Noachis Terra. Similar to those outcrops in Noachis Terra, the material observed in this location appears to be exposed from beneath a dark-toned cap rock, which is inferred to be basaltic material that was emplaced by volcanic resurfacing. This capping unit shows evidence of aeolian deflation, meaning that it has been eroded by wind over time, resulting in the exposure of the underlying light-toned layer, which is demarcated by a white arrow in Figure 11A. In Figure 11B the extent of the feldspathic material is shown in red, and is skirted by material that appears yellow in the CUSTOM 2c browse product, which indicates something of a spectral convolution between a characteristic feldspar spectrum and an olivine spectrum with a broad absorption occurring around 1.0 μm. One speculative interpretation of this is that Fe^{2+}-rich waters percolated through the plagioclase-rich material thereby replacing its Ca^{2+} ions, then emplaced them in the olivine below (in its M2 site within its orthosilicate structure, typically filled by ferrous iron), which could be why the spectral signature of olivine here does not resemble a typical Fe-olivine and has a broader absorption shifted to longer wavelengths due to Fe^{2+} concentrated in the M1 site; the feature near 1.0 μm attributed to Fe^{2+} in the M2 site would be drastically subdued by the substitution of Ca^{2+} [Sunshine and Pieters, 1998]). The material that is greener in color is more spectrally consistent with typical Fe-olivine.

The spectra corresponding to the central and eastern portion of the light-toned outcrop are shown in Figure 12A. The two spectra appear to be very similar, with a possible shift to shorter wavelengths of the central absorption for the green spectrum and the presence of what could be a feature attributed to hydration (~1.9 μm). This outcrop is spectrally interpreted as predominately composed of Ca-rich plagioclase, although when comparing to USGS spectral library endmembers of the plagioclase and alkali feldspar series (i.e., Ca-plagioclase and Fe^{2+}-containing K-feldspar, respectively) the determination does not seem as straightforward as presented in previous studies. We therefore allow for a broader range of compositional interpretations of this outcrop and the examples identified by Wray et al. (2013), who invoked a felsic composition. There were no alteration products identified in this scene.

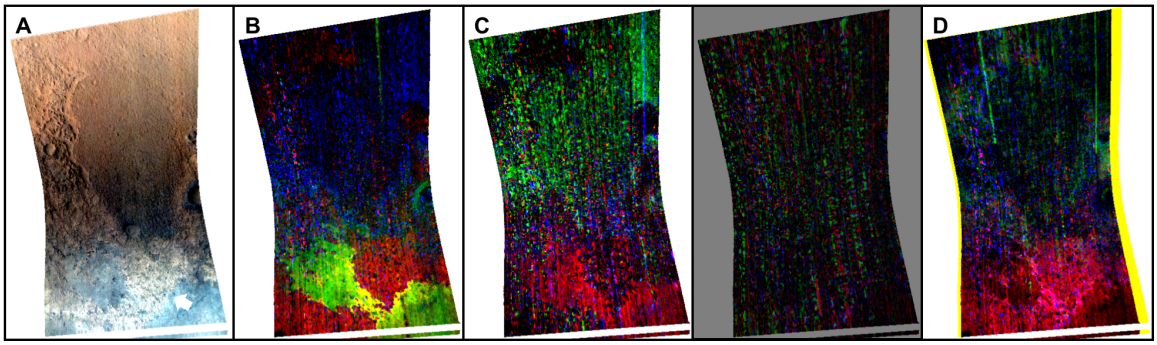

Figure 11: (A) shows an enhanced true color representation of HRL0001C492, while the following browse product maps allow for the visualization of the sizeable outcrop of fractured light-toned material, which is indicated by a white arrow. (B) and (C) reveal the relationship between material enriched in feldspar and phases that are more mafic, while (D) displays the distribution of structurally bound water within the scene and possible hydration features associated with feldspar. The browse products being shown here are TRU (A), CUSTOM 1 (B), MAF (C), and CUSTOM 2c (D).

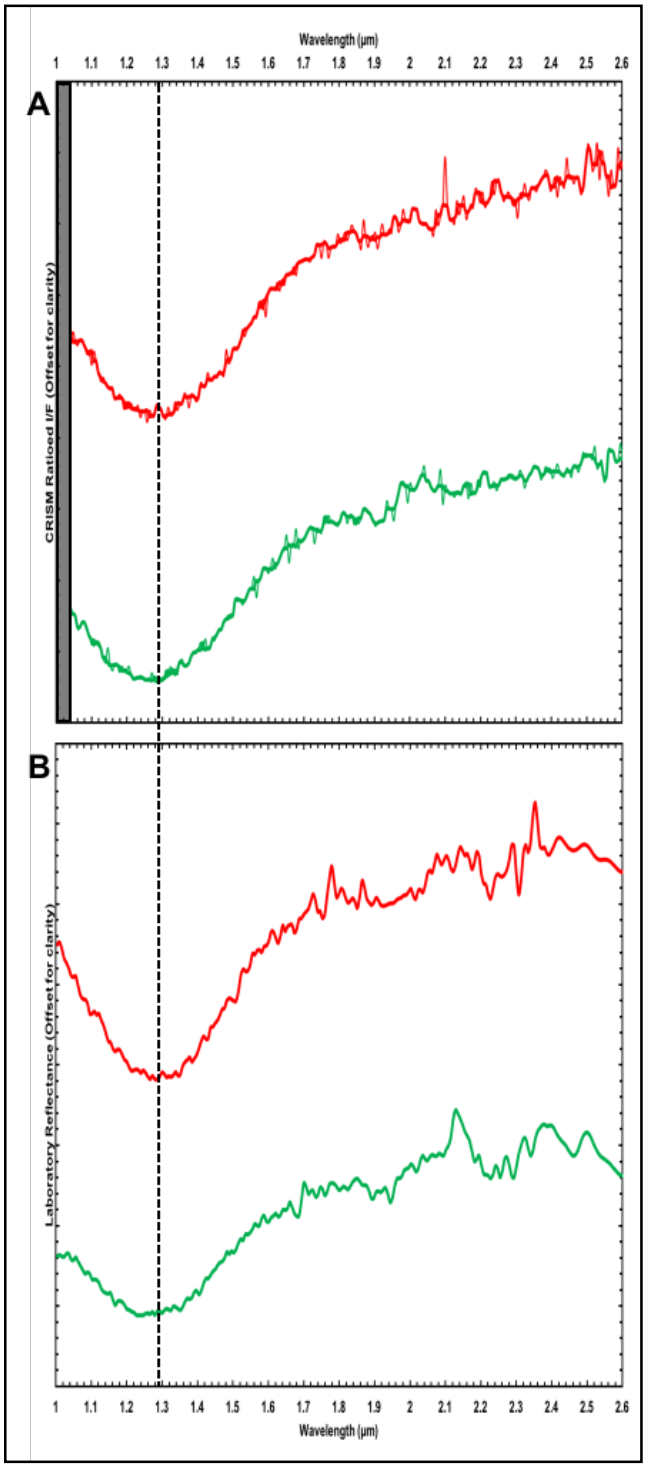

Figure 12: (A) CRISM ratioed I/F spectra from HRL0001C492 (fractured light-toned layer exposed within the southern portion of an unnamed crater) in southwestern Terra Cimmeria. The red and green colored spectra from panel A were collected from different regions on the exposure and seem to show a similar absorption at ~1.28 μm. (B) Comparable USGS library spectra for anorthite (Ca-rich endmember, red spectrum) and Fe-rich orthoclase (K-rich endmember of the alkaline feldspar series, green spectrum). All spectra are vertically offset for clarity and the gray box denotes where spectral data was removed due to the VNIR-IR detector boundary-related issue mentioned previously (1 to ~1.04 μm).

3.2.3.2 Crater 30 (Unnamed)

The observation analyzed here, FRT0001191E, shows two craters that have impacted a flat-floored crater with a heavily degraded rim that is about 76 km in diameter. This observation represents the farthest east that feldspathic material was identified within the defined region of study. The spectra collected from this image are from the regions marked by the two white arrows in Figure 13A, which are both located just outside of the rims of the craters shown below. In Figure 14, the red spectrum indicates a material that is slightly hydrated and appears as a bright white color in Figure 13D, while the green spectrum shows an unaltered material, which appears red in Figure 13B and yellow in Figure 13D. The fact that the feldspar-rich material in panel D appears yellow instead of red can be explained by its also containing bound H_2O, which is what the BD3000 parameter detects. However, this region was not highlighted by our parameters sensitive to hydration features near 1.9 μm.

Since these two small craters are in close proximity to one another, they can help us understand the stratigraphy of the infill material. As stated previously, a large majority of these larger infilled craters are capped by material more mafic in composition, which is confirmed spectrally here in crater 30 by the presence of olivine and high-calcium pyroxene within the ejecta of the small crater in Figure 13A. These mafic materials can be seen north of the larger crater imaged in the scene, and also in a spectrally distinct layer located within this larger crater (halfway down the crater wall), shown as cyan (high-Ca pyroxene/olivine) and green (mostly olivine) in Figure 13B. This material is representative of Hesperian-aged lava flows [Mustard et al., 2005; Bibring et al., 2006] that have capped many similar infilled craters within the study region. The most interesting material spectrally resolved in this image was the excavated material

deposited closest to the crater rims, which typically represents the deepest layers exposed by the impacts. Two spectrally distinguishable layers were exposed. The material from the smaller of the two craters imaged appears to overlie the material exhumed by and deposited closest to the larger crater. Therefore, we postulate that the hydrated feldspar-rich material is underlying the unaltered feldspar-rich material within the stratigraphic column of crater infill. The significance of this will be briefly discussed in the subsequent chapter. The relationship between hydration/alteration state seen at this site is consistent with the trend seen at the previously discussed site in that as the feldspar-bearing material is altered, the ferrous iron absorption feature seems to migrate to shorter wavelengths and decrease in breadth. However, as mentioned before, the significance of this change in the position of the center of the characteristic absorption is not yet completely understood, and could possibly be due to decrease in FeO content, change in chemical composition (i.e., from Ca to Na to even alkali-feldspar), or decrease in grain size.

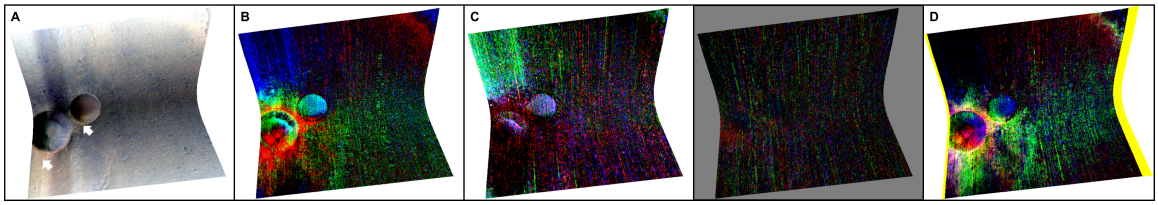

Figure 13: (A) shows an enhanced true color representation of FRT0001191E, while the remaining browse product maps allow for visualization of the spectrally distinct ejecta and material immediately surrounding the rims of the craters. ROIs are indicated by white arrows. (B) and (C) reveal the relationship between material enriched in feldspar and phases that are more mafic, while (D) displays the distribution of structurally bound water within the scene and possible hydration features associated with feldspar. The browse products being shown here are the same as in Figure 11.

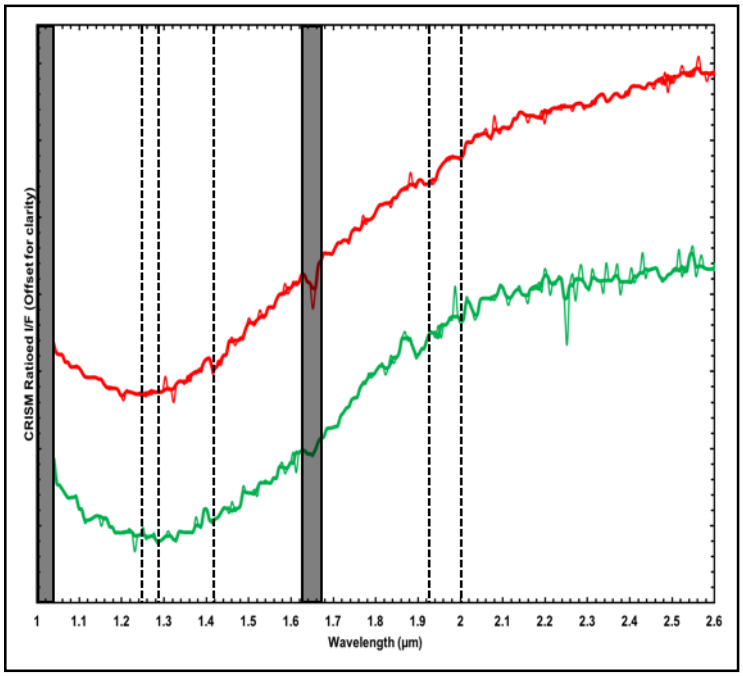

Figure 14: Ratioed CRISM I/F spectra from the two regions identified by white arrows in panel A of Figure 13. This observation is located within a substantially infilled, degraded crater in western Cimmeria Terra. The red spectrum shows a slightly hydrated feldspar-rich material, while the green spectrum is more indicative of an unaltered feldspar spectrum. The spectra presented here are offset for clarity and the gray boxes indicate where spectral data was disregarded due to detector boundary-related issues (1 to ~1.04 μm and ~1.65 μm). The dotted lines indicate characteristic absorptions.

CHAPTER 4: DISCUSSION

4.1 Possible Formation Environment and Mechanism of Observed Feldspathic Material

4.1.1 Feldspathic Material in Infilled Flat-floored Craters

As discussed in the prior chapter, the CRISM observations in crater 2, crater 22, and crater 30 represent the three sites within the region of study where feldspar-bearing material was observed within the stratigraphy of infilled flat-floored craters. One of these occurrences was observably altered to (Fe,Mg)-phyllosilicates (specifically, (Fe,Mg)-smectites) and in association with several other hydrated phases within the imaged area. All three craters appear to be capped with a Hesperian-aged, spectrally bland, dark-toned unit that exhibits little to no signs of alteration and appears slightly pyroxene-rich spectrally (as demonstrated visually in panels B and C of Figures 6, 10, and 12).

The scene containing the altered feldspathic material, imaged by FRT00009665, shows a wide array of minerals (e.g., (Al,Fe,Mg)-phyllosilicates, hydrated silica, and mafics that compose the caprock) that could be used to better constrain the environments in which the feldspar had formed and has since been altered. The phyllosilicates found within this scene appear to be stratified, with the Al-phyllosilicates (e.g., Al-smectites and kaolins) with/or without sedimentary hydrated silica overlying the (Fe,Mg)-phyllosilicates (e.g., (Fe,Mg)-smectites) imaged in the northeastern portion of the scene. This stratigraphy is consistent with that seen in several studies that have previously reported a similar layered phyllosilicate sequence on Mars, including in Mawrth Vallis (and surrounding regions), Nili Fossae, and exposures prevalent

throughout Noachian-aged terrain [Murchie et al., 2009a; Mustard et al., 2009; Wray et al., 2009; Ehlmann et al., 2011b]. These layered sedimentary deposits were emplaced during the early to late Noachian and indicate a relatively long-lasting period in Martian history where surficial, or near-surficial, neutral to alkaline pH aqueous alteration conditions were widespread [Bibring et al., 2006]. Currently, a leading hypothesis is that these materials were a result of pedogenic weathering of basaltic terrains or alteration of volcanic ash [Murchie et al., 2009a], but the association of feldspar-rich material with (Al,Fe,Mg)-smectites found in this particular observation suggests that the material that was altered to form these phyllosilicates may have been more feldspathic in composition. However, these clay minerals could alternatively have been formed principally at depth by one of three different mechanisms (i.e., magmatic hydrothermal activity, crater impact-related aqueous alteration, or via heat supplied crustal cooling). The exact mechanism of formation is unclear, but from comparison of the spectra in Figure 8 it can be suggested that the altered material may contain a Na-rich plagioclase, which remained after alteration of the more calcic feldspar present in the adjacent unaltered feldspar-bearing material. The presence of hydrated silica and Al-rich clays in the scene could also suggest that a more felsic layer was originally present overlying the (Fe,Mg)-smectite layer; silica and Al-clays could thus have been alteration products of a more silica-rich (possibly, felsic to intermediate) parent material present at the Martian surface. It is also possible that the parent material was originally a porphyritic basalt with plagioclase phenocrysts [Rogers and Nekvasil, 2015] that was subsequently altered to a rock composed of (Fe,Mg)-smectite and Na-rich plagioclase, which would presumably be more stable at the surface conditions of Mars at the time of formation.

The observations from the other two craters binned into this category (HRL0001C492 and FRT0001191E) both show no spectral evidence of alteration

products. HRL0001C492 reveals a fractured, light-toned outcrop being exposed beneath the aforementioned darker caprock. Underlying the feldspar-bearing material is a skirting material interpreted as a unit enriched in Ca-rich olivine, as spectrally described earlier, which in turn borders (and appears to overlie) a material spectrally dominated by Fe-olivine. Possible formation mechanisms for this particular outcrop include those inferred from other similar outcrops reported in Noachis Terra and Nili Patera by Wray et al. (2013): (1) feldspar-rich crater floors could have been emplaced through partial melting of basaltic crust and slow cooling with crystal density separation similar to the formation of anorthosite plutons on Earth [Carter and Poulet, 2013], or (2) crater floor high-silica bedrock could have been exhumed or re-melted and extruded via impact-generated fractures in basement [Edwards et al., 2009]. These outcrops could also be sedimentary in nature resulting from the weathering, transport, and subsequent lithification of igneous materials or the emplacement and consolidation of volcanic material (e.g., tuff). The second observation, FRT0001191E, reveals the presence of feldspathic material within the ejecta deposited closest to the rims of two small craters on the larger crater floor. Indeed, this ejected material likely represents some of the oldest material contained within this infilled crater. The stratigraphy of this infill can be observed in the wall of the larger superposed crater, showing that the hypothesized feldspar-rich layer is overlain by a high-calcium pyroxene/olivine dominated layer, which in turn is capped by a relatively bland unit that appears to have a negligible pyroxene component. The feldspathic material here appears to be both hydrated and unaltered, with one overlying the other or occurring within a single layer. The material itself does not appear to have originated from a thick extensive unit like the one seen in Noachis but from a less consolidated layer, consistent with a more sedimentary interpretation rather than igneous. This crater also represents the easternmost extent of feldspar-bearing material identified, and it is located to the southwest of Gale crater where felsic float material was found and

chemically analyzed in situ [Sautter et al., 2015]. Further exploration of the intervening terrain in search of additional feldspathic materials that might link these two sites would be worthwhile.

4.1.2 Feldspathic Material in Central Peaks of Complex Craters

The origin and formation of the feldspar-rich material in this observation may be easier to understand and have fewer alternate formation scenarios. As has been previous discussed, the feldspathic material observed in FRT00009E58 is most certainly co-occurring with analcime in rock fragments distributed throughout the imaged central peak region, based on the position of unique spectral features of this Na-zeolite as described in previous chapters. Analcime can form in a wide array of geologic environments, with the examples most relevant to Mars being (1) saline, alkaline lacustrine environments, (2) soils and land surfaces, (3) low-temperature open to closed tephra systems, (4) burial diagenesis, or (5) hydrothermal alteration [Hay and Sheppard, 2001].

The first of our two preferred interpretations for this exhumed fragmented material on Mars is the scenario wherein silica-rich volcanic glass was altered by saline, alkaline waters to form smectites (of the Al, Fe, and/or Mg-variety), nonanalcimic zeolites, analcime, and alkali feldspar (both Na and K-rich endmembers). These deposits are usually mineralogically zoned, with the first phase to form being smectites and the last to precipitate from the pore fluid being alkali feldspar. Preliminary spectral analysis of this central uplift revealed the presence of all the previously listed phases, with analcime occurring in mixtures that include both (Fe,Mg)-smectite-analcime and (Na,K)-feldspar-analcime in the exposed blocks. There are many different combinations

in which this type of zonation can occur; a summary of Earth analogue localities can be found in [Hay and Sheppard, 2001]. This zoning is controlled by increasing salinity and represented by a series of reactions that go from silicic vitric material to open-framework zeolite (nonanalcimic) to analcime to alkali-feldspar. The second possible formation mechanism for the feldspar-analcime material is in the form of low-temperature, aqueous alteration of silicic tephra. The end products of this reaction are ultimately the same as mentioned for the first formation environment, but hydrated silica is also a product that is observed terrestrially in these systems. Also, the aqueous reaction that converts glass to smectite causes an increase in the concentration of dissolved silica in the solution, thereby making conditions favorable for zeolite formation.

A sodic to potassic composition for the feldspar-related absorption feature seen in Figure 10 (both red and green spectra) is invoked both due to common occurrence between analcime and alkali-feldspars and (to a lesser extent) the position of the absorption feature at roughly 1.25 μm. However, more calcic plagioclase could also be present, but no prior relevant research could be found citing the occurrence of Ca-rich feldspar with analcime. Yet hydrothermal alteration cannot be excluded as a possible formation mechanism of this material; for comparison, Ehlmann et al. (2009) found analcime in a similar geological context (i.e., exposed in a central peak) and noted the similarity of that mineral assemblage to those resulting from the hydrothermal alteration of target material within a terrestrial impact crater [e.g., Allen et al., 1982; Naumov, 2005].

CHAPTER 5: Conclusion

In summary, the work presented here demonstrates the need to reevaluate the widely accepted idea that Mars is a terrestrial body dominated by basaltic compositions and their expected alteration products. It illustrates the need to further our understanding of how the composition of feldspar dictates its spectral fingerprint (e.g., to what extent does the substitution of Fe^{2+} for Ca^{2+} within the structure of an alkali feldspar affect the position and depth of the characteristic ferrous iron related absorption at ~1.25 μm). In this study, a tentative relationship between hydration/alteration state and, possibly, the composition of feldspar has been shown in that the absorption associated with feldspar shifts to shorter wavelengths and becomes narrower when feldspar is altered to (Al,Fe,Mg)-smectites or when feldspar is occurring with a hydrated phase such as the zeolite analcime. Previously reported trends suggest that FeO content, grain size, and composition of feldspar all play a role in determining the center of the spectral absorption, so further laboratory work is needed to ascertain if these effects can be deconvolved. Also new in this study are four previously unidentified, spectrally confirmed occurrences of feldspar-rich material within the defined study region. One of these is texturally similar to previous exposures documented in Noachis Terra, with the other three appearing dissimilar to anything presented thus far. The identification of feldspar-rich material, which may have been emplaced by sedimentary processes, in Cimmeria Terra drastically increases the possible spatial extent of feldspathic material across the Martian surface, and is the closest identification, geographically, to the in situ detection of high silica, high alkali feldspar enriched float rock located within the confines of Gale crater.

REFERENCES

Adams, J. B. (1975). Interpretation of visible and near-infrared diffuse reflectance spectra of pyroxenes and other rock-forming minerals. In C. Karr Jr. (Ed.), *Infrared and Raman spectroscopy of lunar and terrestrial minerals* (pp. 91-116). New York, NY: Academic Press.

Adams, J. B., and Goullaud, L. H. (1978). Plagioclase feldspars: Visible and near infrared diffuse reflectance spectra as applied to remote sensing. *Proceedings of the Ninth Lunar and Planetary Science Conference*, *9*, 2901-2909.

Allen, C. C., Gooding, J. L., and Keil, K. (1982). Hydrothermally altered impact melt rock and breccia: Contributions to the soil of Mars. *Journal of Geophysical Research: Solid Earth*, *87*(B12), 10083-10101, doi:10.1029/JB087iB12p10083.

Bandfield, J. L., Hamilton, V. E., and Christensen, P. R. (2000). A global view of Martian surface compositions from MGS-TES. *Science*, *287*(5458), 1626-1630, doi:10.1126/science.287.5458.1626.

Bandfield, J. L. (2002). Global mineral distributions on Mars. *Journal of Geophysical Research: Planets*, *107*(E6), 5042, doi:10.1029/2001JE001510.

Bandfield, J. L., et al. (2004). Identification of quartzofeldspathic materials on Mars. *Journal of Geophysical Research: Planets*, *109*, E10009, doi:10.1029/2004JE002290.

Bandfield, J. L. (2006). Extended surface exposures of granitoid compositions in Syrtis Major, Mars. *Geophysical research letters*, *33*, L06203, doi:10.1029/2005GL025559.

Bandfield, J. L. (2008). High-silica deposits of an aqueous origin in western Hellas Basin, Mars. *Geophysical Research Letters*, *35*, L12205, doi:10.1029/2008GL033807.

Bibring, J. P., et al. (2005). Mars surface diversity as revealed by the OMEGA/Mars Express observations. *Science*, *307*(5715), 1576-1581, doi:10.1126/science.1108806.

Bibring, J. P., et al. (2006). Global mineralogical and aqueous Mars history derived from OMEGA/Mars Express data. *science*, *312*(5772), 400-404, doi:10.1126/science.1122659.

Bishop, J., Murad, E., and Dyar, M. D. (2002). The influence of octahedral and tetrahedral cation substitution on the structure of smectites and serpentines as observed through infrared spectroscopy. *Clay Minerals*, *37*(4), 617-628, doi:10.1180/0009855023740064.

Bishop, J. L., et al. (2008a). Reflectance and emission spectroscopy study of four groups of phyllosilicates: Smectites, kaolinite-serpentines, chlorites and micas. *Clay Minerals*, *43*(1), 35-54, doi:10.1180/claymin.2008.043.1.03.

Bishop, J. L., et al. (2008b). Phyllosilicate diversity and past aqueous activity revealed at Mawrth Vallis, Mars. *Science*, *321*(5890), 830-833, doi:10.1126/science.1159699.

Bristow, T. F., and Milliken, R. E. (2011). Terrestrial perspective on authigenic clay mineral production in ancient martian lakes. *Clays and Clay Minerals*, *59*(4), 339-358, roi:10.1346/CCMN.2011.0590401.

Burns, R. G. (2005). *Mineralogical applications of crystal field theory* (Vol. 5) (2nd ed.). A. Putnis and R. C. Liebermann (Eds.). New York, NY: Cambridge University Press.

Carr, M. H., and Head, J. W. (2010). Geologic history of Mars. *Earth and Planetary Science Letters*, *294*(3-4), 185-203, doi:10.1016/j.epsl.2009.06.042.

Carter, J., et al. (2013). Hydrous minerals on Mars as seen by the CRISM and OMEGA imaging spectrometers: Updated global view. *Journal of Geophysical Research: Planets*, *118*(4), 831-858, doi:10.1029/2012JE004145.

Carter, J., and Poulet, F. (2013). Ancient plutonic processes on Mars inferred from the detection of possible anorthositic terrains. *Nature Geoscience*, *6*(12), 1008-1012, doi:10.1038/ngeo1995.

Ceamanos, X., and Douté, S. (2010). Spectral smile correction of CRISM/MRO hyperspectral images. *IEEE Transactions on Geoscience and Remote Sensing*, *48*(11), 3951-3959, doi:10.1109/TGRS.2010.2064326.

Cheek, L. C., et al. (2013). The distribution and purity of anorthosite across the Orientale basin: New perspectives from Moon Mineralogy Mapper data. *Journal of Geophysical Research: Planets*, *118*(9), 1805-1820, doi:10.1002/jgre.20126.

Christensen, P. R., et al. (2000). Identification of a basaltic component on the Martian surface from Thermal Emission Spectrometer data. *Journal of Geophysical Research*,*105*(E4), 9609-9621, doi:10.1029/1999JE001127.

Christensen, P. R., et al. (2005). Evidence for magmatic evolution and diversity on Mars from infrared observations. *Nature*, *436*(7050), 504-509, doi:10.1038/nature03639.

Clark, R. N., and Roush, T. L. (1984). Reflectance spectroscopy: Quantitative analysis techniques for remote sensing applications. *Journal of Geophysical Research: Solid Earth*, *89*(B7), 6329-6340, doi:10.1029/JB089iB07p06329.

Clark, R. N., et al. (1990). High spectral resolution reflectance spectroscopy of minerals. *Journal of Geophysical Research: Solid Earth*, *95*(B8), 12653-12680, doi:10.1029/JB095iB08p12653.

Clark, R. N. (1999). Spectroscopy of rocks and minerals, and principles of spectroscopy. In A. N. Rencz (Ed.), *Manual of Remote Sensing: Remote Sensing for the Earth Sciences* (Vol. 3) (3rd ed.) (pp. 3-58). New York, NY: John Wiley & Sons.

Clark, R.N., et al., 2007, USGS digital spectral library splib06a: U.S. Geological Survey, Digital Data Series 231.

Cloutis, E. A., et al. (2000). Hydrated carbonate minerals: Spectral reflectance properties and possibility of detection in Martian spectra. *Lunar Planet. Sci. Conf. XXXI*, Abstract 1152.

Cloutis, E. A., Asher, P. M., and Mertzman, S. A. (2002). Spectral reflectance properties of zeolites and remote sensing implications. *Journal of Geophysical Research: Planets*, *107*(E9), 5067, doi:10.1029/2000JE001467.

Crown, D. A., and Pieters, C. M. (1987). Spectral properties of plagioclase and pyroxene mixtures and the interpretation of lunar soil spectra. *Icarus*, *72*(3), 492-506, doi:10.1016/0019-1035(87)90047-9.

Deer, W. A., Howie, R. A., and Zussman, J. (2001). *Rock-Forming Minerals: Framework Silicates – Feldspars* (Vol. 4A) (2nd ed.). Bath, UK: The Geological Society of London.

Ding, N., et al. (2015). The central uplift of Ritchey crater, Mars. *Icarus*, *252*, 255-270, doi:10.1016/j.icarus.2014.11.001.

Edwards, C. S., et al. (2009). Global distribution of bedrock exposures on Mars using THEMIS high-resolution thermal inertia. *Journal of Geophysical Research: Planets*, *114*, E11001, doi:10.1029/2009JE003363.

Ehlmann, B. L., et al. (2008). Orbital identification of carbonate-bearing rocks on Mars. *Science*, *322*(5909), 1828-1832, doi:10.1126/science.1164759.

Ehlmann, B. L., et al. (2009). Identification of hydrated silicate minerals on Mars using MRO-CRISM: Geologic context near Nili Fossae and implications for aqueous alteration. *Journal of Geophysical Research: Planets*, *114*, E00D08, doi:10.1029/2009JE003339.

Ehlmann, B. L., et al. (2011a). Evidence for low-grade metamorphism, hydrothermal alteration, and diagenesis on Mars from phyllosilicate mineral assemblages. *Clays and Clay Minerals*, *59*(4), 359-377, doi:10.1346/CCMN.2011.0590402.

Ehlmann, B. L., et al. (2011b). Subsurface water and clay mineral formation during the early history of Mars. *Nature*, *479*(7371), 53-60, doi:10.1038/nature10582.

Ehlmann, B. L., et al. (2013). Geochemical consequences of widespread clay mineral formation in Mars' ancient crust. *Space Science Reviews*, *174*(1-4), 329-364, doi:10.1007/s11214-012-9930-0.

Ehlmann, B. L., and Edwards, C. S. (2014). Mineralogy of the Martian surface. *Annual Review of Earth and Planetary Sciences*, *42*, 291-315, doi:10.1146/annurev-earth-060313-055024.

Filiberto, J., et al. (2014). Gabbroic Shergottite Northwest Africa 6963: An intrusive sample of Mars. *American Mineralogist*, *99*(4), 601-606, doi:10.2138/am.2014.4638.

Hay, R. L., and Sheppard, R. A. (2001). Occurrence of zeolites in sedimentary rocks: an overview. *Reviews in mineralogy and geochemistry*, *45*(1), 217-234, doi:10.2138/rmg.2001.45.6.

Horgan, B. (2013). Planetary science: Evolved magma on Mars. *Nature Geoscience*, *6* (12), 991-992, doi:10.1038/ngeo2010.

Horgan, B. H. N., et al. (2014). Near-infrared spectra of ferrous mineral mixtures and methods for their identification in planetary surface spectra. *Icarus*, *234*, 132-154, doi:10.1016/j.icarus.2014.02.031.

Humayun, M., et al. (2013). Origin and age of the earliest Martian crust from meteorite NWA [thinsp] 7533. *Nature*, *503*(7477), 513-516. doi:10.1038/nature12764.

Malin, M. C., et al. (2007). Context camera investigation on board the Mars Reconnaissance Orbiter. *Journal of Geophysical Research: Planets*, *112*, E05S04, doi:10.1029/2006JE002808.

McEwen, A. S., et al. (2007). Mars reconnaissance orbiter's high resolution imaging science experiment (HiRISE). *Journal of Geophysical Research: Planets*, *112*, E05S02, doi:10.1029/2005JE002605.

McGuire, P. C., et al. (2009). An improvement to the volcano-scan algorithm for atmospheric correction of CRISM and OMEGA spectral data. *Planetary and Space Science*, *57*(7), 809-815, doi:10.1016/j.pss.2009.03.007.

McSween, H. Y., Taylor, G. J., and Wyatt, M. B. (2009). Elemental composition of the Martian crust. Science, 324(5928), 736-739, doi:10.1126/science.1165871.

McSween, H. Y., Labotka, T. C., and Viviano-Beck, C. E. (2015). Metamorphism in the martian crust. *Meteoritics & Planetary Science*, *50*(4), 590-603, doi:10.1111/maps.12330.

Milliken, R. E., et al. (2008). Opaline silica in young deposits on Mars. *Geology*, *36*(11), 847-850, doi:10.1130/G24967A.1.

Morgan, F. (2011). Improved algorithm for CRISM volcano scan atmospheric correction. *Lunar Planet. Sci. Conf. XLII*, Abstract 2453.

Murchie, S., et al. (2007). Compact reconnaissance imaging spectrometer for Mars (CRISM) on Mars reconnaissance orbiter (MRO). *Journal of Geophysical Research: Planets*, *112*, E05S03, doi:10.1029/2006JE002682.

Murchie, S. L., et al. (2009a). A synthesis of Martian aqueous mineralogy after 1 Mars year of observations from the Mars Reconnaissance Orbiter. *Journal of Geophysical Research: Planets*, *114*, E00D06, doi:10.1029/2009JE003342.

Murchie, S. L., et al. (2009b). Compact Reconnaissance Imaging Spectrometer for Mars investigation and data set from the Mars Reconnaissance Orbiter's primary science phase. *Journal of Geophysical Research: Planets*, *114*, E00D07, doi:10.1029/2009JE003344.

Mustard, J., et al. (1993). The surface of Syrtis Major- Composition of the volcanic substrate and mixing with altered dust and soil. *Journal of Geophysical Research*, *98*(E2), 3387-3400, doi:10.1029/92JE02682.

Mustard, J. F., et al. (2005). Olivine and pyroxene diversity in the crust of Mars. *Science*, *307*(5715), 1594-1597, doi:10.1126/science.1109098.

Mustard, J. F., et al. (2008). Hydrated silicate minerals on Mars observed by the Mars Reconnaissance Orbiter CRISM instrument. *Nature*, *454*(7202), 305-309, doi:10.1038/nature07097.

Nash, D. B., and Conel, J. E. (1974). Spectral reflectance systematics for mixtures of powdered hypersthene, labradorite, and ilmenite. *Journal of Geophysical Research*, *79*(11), 1615-1621, doi:10.1029/JB079i011p01615.

Naumov, M. V. (2005). Principal features of impact-generated hydrothermal circulation systems: mineralogical and geochemical evidence. *Geofluids*, *5*(3), 165-184, doi:10.1111/j.1468-8123.2005.00092.x.

Ohtake, M., et al. (2009). The global distribution of pure anorthosite on the Moon. *Nature*, *461*(7261), 236-240. doi:10.1038/nature08317.

Parente, M. (2008). A new approach to denoising CRISM images. *Lunar Planet. Sci. Conf. XXXIX*, Abstract 2528.

Pelkey, S. M., et al. (2007). CRISM multispectral summary products: Parameterizing mineral diversity on Mars from reflectance. *Journal of Geophysical Research: Planets*, *112*, E08S14, doi:10.1029/2006JE002831.

Popa, C., Esposito, F., and Colangeli, L. (2010). New landing site proposal for Mars Science Laboratory (MSL) in Xanthe Terra. *Lunar Planet. Sci. Conf. XLI*, Abstract 1807.

Poulet, F., et al. (2005). Phyllosilicates on Mars and implications for early Martian climate. *Nature*, *438*(7068), 623-627, doi:10.1038/nature04274.

Rice, M. S., et al. (2013). Reflectance spectra diversity of silica-rich materials: Sensitivity to environment and implications for detections on Mars. *Icarus*, *223*(1), 499-533, doi:10.1016/j.icarus.2012.09.021.

Rogers, A. D., and Nekvasil, H. (2015). Feldspathic rocks on Mars: Compositional constraints from infrared spectroscopy and possible formation

mechanisms. *Geophysical Research Letters*, *42*(8), 2619-2626, doi:10.1002/2015GL063501.

Ruff, S. W., and Christensen, P. R. (2002). Bright and dark regions on Mars: Particle size and mineralogical characteristics based on Thermal Emission Spectrometer data. *Journal of Geophysical Research: Planets*, *107*(E12), 5127, doi:10.1029/2001JE001580.

Sautter, V., et al. (2015). In situ evidence for continental crust on early Mars. *Nature Geoscience*, *8*(8), 605-609, doi:10.1038/ngeo2474.

Seelos, F. P., et al. (2009), CRISM hyperspectral data filtering with application to MSL landing site selection, *Eos Trans. AGU, 90*(52), Fall Meet. Suppl., Abstract P23A-1234.

Seelos, F. P., et al. (2011). CRISM Data Processing and Analysis Products Update – Calibration, Correction, and Visualization. *Lunar Planet. Sci. Conf. XLII*, Abstract 1438.

Serventi, G., et al. (2013). Spectral variability of plagioclase–mafic mixtures (1): Effects of chemistry and modal abundance in reflectance spectra of rocks and mineral mixtures. Icarus, 226(1), 282-298, doi:10.1016/j.icarus.2013.05.041.

Skok, J. R., et al. (2010). Silica deposits in the Nili Patera caldera on the Syrtis Major volcanic complex on Mars. *Nature Geoscience*, *3*(12), 838-841, doi:10.1038/ngeo990.

Smith, M. R., and Bandfield, J. L. (2012). Geology of quartz and hydrated silica-bearing deposits near Antoniadi Crater, Mars. *Journal of Geophysical Research: Planets*, *117*, E06007, doi:10.1029/2011JE004038.

Smith, M. R., Bandfield, J. L., Cloutis, E. A., and Rice, M. S. (2013). Hydrated silica on Mars: Combined analysis with near-infrared and thermal-infrared spectroscopy. *Icarus*, *223*(2), 633-648, doi:10.1016/j.icarus.2013.01.024.

Sunshine, J. M., and Pieters, C. M. (1998). Determining the composition of olivine from reflectance spectroscopy. *Journal of Geophysical Research*, *103*(E6), 13675-13688, doi:10.1029/98JE01217.

Viviano-Beck, C. E., et al. (2014). Revised CRISM spectral parameters and summary products based on the currently detected mineral diversity on Mars. *Journal of Geophysical Research: Planets*, *119*(6), 1403-1431, doi:10.1002/2014JE004627.

Viviano-Beck, C. E., et al. (2017). Compositional and structural constraints on the geologic history of eastern Tharsis Rise, Mars. *Icarus*, *284*, 43-58, doi:10.1016/j.icarus.2016.09.005.

Wray, J. J., et al. (2008). Compositional stratigraphy of clay-bearing layered deposits at Mawrth Vallis, Mars. *Geophysical Research Letters*, *35*(12), doi:10.1029/2008GL034385.

Wray, J. J., et al. (2009). Diverse aqueous environments on ancient Mars revealed in the southern highlands. *Geology*, *37*(11), 1043-1046, doi:10.1130/G30331A.1.

Wray, J. J., et al. (2013). Prolonged magmatic activity on Mars inferred from the detection of felsic rocks. *Nature Geoscience*, *6*(12), 1013-1017, doi:10.1038/ngeo1994.

Wyatt, M. B., and McSween, H. Y. (2002). Spectral evidence for weathered basalt as an alternative to andesite in the northern lowlands of Mars. *Nature*, *417*(6886), 263-266, doi:10.1038/417263a.